Pyrophosphate-stabilised amorphous calcium carbonate for bone substitution: toward a doping-dependent cluster-based model

Marion Merle, Jérémy Soulié, Capucine Sassoye, Pierre Roblin, Christian Rey, Christian Bonhomme, Christèle Combes

Pyrophosphate-stabilised amorphous calcium carbonate for bone substitution: toward a doping-dependent cluster-based model

Marion Merle[1], Jérémy Soulié[1], Capucine Sassoye[2], Pierre Roblin[3], Christian Rey[1], Christian Bonhomme[2], Christèle Combes[1,*]

1. CIRIMAT, Université de Toulouse, CNRS, TOULOUSE INP - ENSIACET, Toulouse, France
2. Sorbonne Université, CNRS, LCMCP, Paris, France
3. LGC, CNRS, Université de Toulouse, 118 route de Narbonne Bâtiment 2R1, Toulouse, France

*Corresponding author: Christèle Combes
CIRIMAT – ENSIACET
4 allée Emile Monso
31030 Toulouse Cedex 4
France
christele.combes@ensiacet.fr

Abstract

Calcium carbonates and in particular amorphous calcium carbonate (ACC) are of great interest for bone substitution, due to their excellent biocompatibility and ability to release some of the bone mineral constitutive ions. Despite thorough investigations on ACC precipitation mechanism in the presence of a wide variety of additives to stabilise it, their influence on the composition and structuration of the resulting ACC is rarely finely characterised. In this article, pyrophosphate (Py) was studied as additive, due to its calcite inhibitor role and the good bioactive properties it demonstrated *in vitro* and *in vivo*. A series of pyrophosphate-stabilised ACC (PyACC) powders was synthesised by co-precipitation in water with a various amount of Py, and the structure, composition and multiscale organisation of the resulting compounds were thoroughly characterised. XRD, FTIR spectroscopy and FEG-SEM showed a reduction of the amount and size of calcite crystallites when increasing the Py content, crystallites co-existing with an increasing quantity of amorphous phase, up to obtaining fully amorphous materials above a certain Py amount. Beyond the stabilising role of Py, and considering SAXS, PDF and solid-state NMR analyses, we proposed an experimental model for PyACC based on vaterite-like (or proto-vaterite) cluster of 1 nm surrounded by a 2 nm-outer shell containing pyrophosphate ions and pseudo-structural water stabilising the cluster. This comprehensive study and the resulting model are predominant prerequisite to understand the underlying mechanisms of PyACC evolution and could contribute to the rational design of tunable amorphous and bioinspired inorganic bone substitute materials.

Keywords: amorphous calcium carbonate, pyrophosphate, advanced characterisation, cluster model, nanoscale, bone substitutes

Introduction

Calcium carbonate (CC) is used as bone substitute due to its excellent biocompatibility.[1] Both synthetic and natural $CaCO_3$ demonstrate promising results for bioresorption and/or bioactivity properties.[1,2] Indeed, their *in vivo* degradation can provide Ca^{2+} and CO_3^{2-} ions that are both involved as building ions in the formation of biological apatite.[3] Several CC phases are described in the literature: i) anhydrous crystalline phases (calcite, aragonite and vaterite from the most to the least thermodynamically stable in aqueous solutions)[4]; ii) hydrated crystalline phases hemi-[5], mono-, and hexa-hydrated CC ; and iii) amorphous calcium carbonate (ACC). The latter family includes several compounds whose structure and composition can significantly differ depending on the synthesis conditions or the living organism from which they are derived.[6] They generally show enhanced reactivity in aqueous media or when implanted and hence improved bioactivity.[7] Contrary to calcite, undesirable for bone regeneration because of its low solubility limiting its resorption[7] and the poor ability of apatite to nucleate on calcite,[8] ACC demonstrated efficiency for bone remodeling,[9] protein or gene delivery[10,11] or calcium supply.[12]

Several synthesis processes can lead to ACC, the most mentioned being co-precipitation using calcium and carbonate salt precursors in solution.[13,14] The associated formation mechanisms have been described *via* classical and non-classical nucleation theories. The classical pathway for explaining preferential formation of ACC compared to crystalline CC is based either on thermodynamically and kinetically-driven route.[15] The non-classical pathway involves decomposition of the solution containing calcium and carbonate ions into a low concentrated solution and a denser one. This is supported by two sub-theories respectively related to polymer-induced liquid precursors (PILPs)[16,17] and stable pre-nucleation clusters (PNCs).[18,19] PNCs are nanostructures alternating Ca^{2+} and CO_3^{2-} ions in solution that form dense hydrated calcium carbonate nanodroplets, whose aggregation leads to proto-structured ACC clusters.[20] Finally, solid ACC particles are formed by partial dehydration and solidification.[20] The organisation of these clusters is described to be close to those of crystalline lattice of CC phases such as vaterite or calcite and named proto-vaterite or proto-calcite, respectively.[21] As only a few ions are organised within such clusters, they cannot be detected by conventional X-ray diffraction (XRD) but their proto-structure have been characterised by Fourier-transformed infrared (FTIR) spectroscopy,[21,22] nuclear magnetic resonance (NMR),[21,23] pair distribution function (PDF)[24,25] and extended X-ray absorption fine structure (EXAFS).[26,27] Regardless of the nucleation theory, ACC synthesis requires strategies to prevent crystallisation into a more thermodynamically stable phase, especially calcite. This phenomenon may occur through solid-state transformation[28] or dissolution-reprecipitation processes.[29] Hence, various synthesis approaches are described, either kinetically (low temperature often coupled with basic pH[30,31]) or with ionic or molecular additives such as magnesium,[32] citrate[33] or polymers.[17,34] Among these species, phosphate ions are known to be crystallisation inhibitors of biogenic CC,[35] or synthetic calcite.[36] Orthophosphate anions (PO_4^{3-}) have been used in co-precipitation syntheses and showed an improved stabilisation of ACC leading to an increase of its crystallisation temperature.[37] It was proposed that phosphate anions could enhance the formation of a rich solute liquid phase during liquid-liquid separation and stabilise it.[38] They were demonstrated to increase ACC stability by decreasing the size of nanoparticles or by reducing ion mobility when integrated in the bulk.[37] Phosphate ions could also inhibit crystal growth by adsorbing on the particle surface.[36] In addition to monomers, different polyphosphate ions with various chain lengths were studied as stabilising agents. For example, tri-phosphate exhibited some stabilising properties[39] and polyphosphate (around 20 phosphate units)-stabilised ACC demonstrated a good biodegradability, an osteogenic activity as well as the release of bioactive ions (CO_3^{2-}, PO_4^{3-}, Ca^{2+}).[9] To the best of our knowledge, the use of phosphate dimers, *i.e.* pyrophosphate ions ($P_2O_7^{4-}$), as ACC

stabiliser is only mentioned in one article and one patent,[38,40] but the related material was poorly characterised, and the role of pyrophosphate was not really elucidated. Beyond their potential stabilisation properties,[41] pyrophosphate anions could improve ACC bioactivity. As a matter of fact, the interest of pure calcium pyrophosphate materials had been established, through *in vitro,*[42] *in vivo*[43] tests and a clinical trial.[44] Moreover, pyrophosphate ions are hydrolysed *in vivo* by enzymes[42] leading to orthophosphates ions, one of the main "building bricks" for bone apatite. This property is of major interest as the hydrolysis kinetics of pyrophosphate could also delay pyrophosphate-stabilised ACC resorption and subsequent orthophosphate, carbonate and calcium ions release, opening the way to new perspectives for bioactive bone substitute materials with tunable properties.

Consequently, the aim of the present study is to investigate the influence of the pyrophosphate content on the structure, composition and spatial organisation of ACC through the full characterisation of a series of pyrophosphate-doped ACC powders synthesised by precipitation in aqueous solution. To this extent, XRD, FTIR and Raman spectroscopy, BET analyses, ICP-OES spectrometry and chemical analyses, and TGA-DTA were carried out to understand the impact of such a doping on the structure of ACC as well as on its composition. An additional purpose of this article is to determine the multiscale organisation and morphology of pyrophosphate-stabilised ACC *via* advanced characterisation techniques (FEG-SEM, STEM-EDS, SAXS, WAXS and solid-state NMR) and to propose a pertinent experimental model.

Materials and Methods

1. Reagent and precursor salts

Sodium hydrogencarbonate ($NaHCO_3$, VWR, 27778.293, 100.1 %), ^{13}C-enriched sodium carbonate ($Na_2{}^{13}CO_3$, Cambridge IsotopeLab, CLM-306-5, 99 %) (for ^{13}C NMR analyses), calcium nitrate tetrahydrate ($Ca(NO_3)_2.4H_2O$, Merck, 1.02121.9050, 99.0 - 102.0 %), sodium hydroxide (NaOH, VWR, 28244.295, 99 %) and 20% ammonia solution (NH_4OH, VWR, 21188.294, 20.3 % v/v of NH_3) were purchased and used without any further treatment.

Sodium pyrophosphate ($Na_4P_2O_7$) was synthesised by condensation of sodium hydrogenphosphate (Na_2HPO_4, Merck, 1.06586.2500, 99.0 %) during a night at 400°C, following the method of Mayen *et al.*[45] The X-ray diffractogram and FTIR spectrum of the resulting powder are presented in Figure S1**.**

2. Synthesis

ACC was synthesised by double decomposition between a sodium hydrogencarbonate and a calcium nitrate aqueous solutions in presence of *z mol.* % of pyrophosphate (*z*PyACC) (*z*: molar ratio (%) of pyrophosphate on carbonate in the anionic solution). The anionic solution was prepared by dissolving 4.200 g of sodium hydrogencarbonate (50.0 mmol) and 0.133 g*z of sodium pyrophosphate (0.5*z mmol) in 250 mL of deionised water at room temperature under magnetic stirring. The pH of this solution, initially around 8, was adjusted to 12.1 - 12.2 with a 6 M sodium hydroxide solution. The cationic solution was prepared by dissolving 11.810 g of calcium nitrate tetrahydrate (50.0 mmol) in 250 mL of deionised water under magnetic stirring at room temperature. The carbonate solution was then quickly added to the calcium one under magnetic stirring, immediately filtrated under vacuum on a Büchner funnel using two filters discs (Sartorius, grade 391) and washed with an ammonia solution (5 mL of 20 % v/v VWR ammonia solution in 1 L of deionised water). Finally, the precipitate was freeze-dried during 24 h and stored in a freezer at - 21°C.

To study the influence of the amount of pyrophosphate, the initial molar percentage *z* of pyrophosphate with respect to carbonate in solution was equal to 0.0, 1.0, 2.5, 3.5, 5.0 or 10.0 %.

In view to increase the signal to noise ratio of ^{13}C solid-state NMR measurements, we prepared ACC powders stabilised with 5 or 10 % of pyrophosphate and enriched in ^{13}C (5PyACC13 and 10PyACC13). We followed the standard synthesis protocol reported above except that sodium hydrogencarbonate salt was replaced, at the same molar quantity, by a ^{13}C-enriched sodium carbonate ($Na_2{}^{13}CO_3$, Cambridge IsotopeLab, CLM-306-5, 99 %); a lower quantity of sodium hydroxide was necessary to adjust the pH of the obtained anionic solution to 12.1. During vacuum filtration, the precipitate was protected by a parafilm and the obtained lyophilised powder was then stored in a sealed container into the freezer, to avoid or limit carbonate ion exchanges with carbon dioxide from the air. The FTIR spectroscopy characterisation of these ^{13}C-enriched zPyACC samples is presented in the Supporting Note SI-B and Figure S2.

3. Characterisation

Powder XRD analyses were performed using a X-ray diffractometer (Bruker D8 ADVANCE) with a copper anticathode ($\lambda(K\alpha_1)$ = 1.54060 Å, $\lambda(K\alpha_2)$ = 1.54439 Å), and a step size of 0.021° between 20° and 80°. Samples were gently crushed with a mortar prior analysis. Crystallite size was calculated using the Debye-Scherrer equation on the (110) calcite peaks, and with a form factor *k* of 0.94.

FTIR spectroscopy analyses were run in transmission mode on samples included in KBr pellets. The spectra were collected with a Nicolet iS50 spectrometer (ThermoElectron), from 400 to 4000 cm^{-1} (64 scans, resolution 4 cm^{-1}).

The calcium content was determined using the complexometry titration method with EDTA and Eriochrome Black T as an indicator.

The carbonate content of zPyACC powders was evaluated using a CO_2 coulometer (Coulometrics, USA) that measures in a closed circuit the CO_2 released during ACC dissolution in an acid solution ($HClO_4$, 2 M).

The phosphorus concentration in pyrophosphate-doped ACC powders was determined by visible spectrophotometry at 460 nm (Shimadzu UV1800) of the phospho-vanado-molybdenum complex; the pyrophosphate ions were fully hydrolysed into orthophosphate in acid solution at 90 °C prior analysis.

Inductive coupled plasma-optical emission spectroscopy ICP-OES (Spectro-Arcos) was used to determine the sodium content in the synthesised zPyACC powders (λ_{Na} = 589 nm) previously dissolved in an aqueous acidic solution (50.0 mg ACC and 3 % m/m HNO_3 in 50 mL of ultrapure water).

Thermogravimetric analyses (TGA) and differential thermal analyses (DTA) were performed with a Setaram instrument (Setsys system) from 25 to 800 °C with a heating rate of 7 °C/min under an air flow.

Powder specific surface area (SSA) was determined according to Brunauer-Emmett-Teller (BET) method using N_2 adsorption measurements on a Tristar II 3020 device. After preliminary tests, the degassing conditions prior the measurements were set to 2 h at 50 °C. Uncertainties were calculated based on the apparatus errors and the uncertainties on the weighted mass.

Scanning transmission electron microscopy (STEM) analysis was done on ultramicrotomy sections of zPyACC powder dispersed in a cross-linked resin and deposited on copper grids. A carbon layer was deposited on the grids before observation. A TEM-ARM (JEM-ARM200F Cold FEG) was used for

imaging, with an acceleration voltage of 80 kV. This observation was coupled with chemical composition analyses by energy-dispersive X-ray spectroscopy (EDS), with an exposition time of ~ 6 min (60 frames).

Images of field emission gun-scanning electron microscopy were acquired on a FEG-SEM JEOL JSM 7800F Prime device, on carbon-taped zPyACC powder samples after a platinum sputtering to limit the accumulation of electrons.

Small-angle X-ray scattering (SAXS) analyses were carried out using a XEUSS 2.0 device with a copper X-ray source at the wavelength λ = 1.5 Å. The record was done at three powder-receptor distances: high distance = 2506.5 mm (from 0.0028 to 0.2 $Å^{-1}$), middle distance = 1216.5 mm (from 0.005 to 0.5 $Å^{-1}$), and short distance = 188 mm (from 0.02 to 3 $Å^{-1}$) in order to obtain a large q-range (from 0.0028 to 3 $Å^{-1}$). The samples were placed in a sample holder where the powder was placed between two layers of Kapton with a thickness equal to 1 mm. SASView software was used for the analysis of SAXS data (http://www.sasview.org/). The determination of the first characteristic dimension was done calculating the intersection point of the equation of the two power laws fitting to the curve before (6 first points) and after the inflexion point, with equation $I(q) = k.q^{-p}$, where k and p can be obtained by the fit. Then, the intersection point of both slopes corresponds to $q_i = 2\pi/D_1$ and the first dimension D_1 of the larger objects could be determined. The second characteristic size was determined *via* the maximum of intensity, which can be highlighted by subtracting the contribution of the second power law. A sphere-hardsphere model was applied, with equation: $I(q) = P(q).S(q)$; the shape factor of sphere being $P(q) = \frac{vol_{fraction}}{V} . \left[3V\Delta\rho \frac{\sin(qr)-qr\cos(qr)}{(qr)^3}\right]^2$, with V volume of the scatterer, $vol_{fraction}$ the volume fraction, $\Delta\rho$ the difference between the sphere-solvent scattering length densities and r the radius of the sphere; and the structure factor $S(q)$ corresponding to the inter-sphere interactions. More information about the fitting processing of the SAXS data are given in Supporting Note SI-G.

X-ray total scattering data (WAXS) were measured for PDF analysis with a Bruker D8 ADVANCE diffractometer equipped with a Göbel mirror and a LYNXEYE high energy detector, with Mo K_α radiation (mean $\lambda(K_{\alpha1\alpha2})$ = 0.71073 Å) at room temperature. Few tens of milligrams of powder were placed in a thin-walled (0.01 mm) borosilicate glass capillary of 1.0 mm diameter. Measurements were performed from Q_{min} = 0.12 $Å^{-1}$ to Q_{max} = 17.0 $Å^{-1}$ (Q = 4πsin(θ)/λ) on rotating capillaries with evolving counting parameters as a function of Q-range in order to optimise the counting rate at high Q. The final XRD diagram was thus obtained from the combination of 7 patterns, converted in counts per second, with the following parameters 2θi(°)-2θf(°)-step size(°)-step time(s): 0.8-31-0.02-2, 29-61-0.04-6, 59-91-0.06-15, 89-121-0.1-40 (twice) and 119-150-0.1-100 (twice) for a total measuring time of 34 hours. Additional scattering measurements from empty capillary were performed in the same conditions for background subtraction. Raw data were treated using the PDFgetX3 program[46] to obtain the experimental $G_{exp}(r)$ function, using the following parameters: Q_{min} = 0.5 $Å^{-1}$, Q_{max} = 17 $Å^{-1}$, r_{poly} = 1.7. PDFGUI software[47] was used to calculate the *Gcalc(r)* functions from structural models. It allowed us to refine the crystalline calcite and vaterite structures from powders specifically synthesised as reference compounds (Supporting Note SI-H1). The refined parameters (cell parameters, isotropic atomic displacements, atomic positions, broadening factors) were then used combined with a dampening factor of 9 Å to mimic the organisation of amorphous phases at small distances.

All solid-state NMR spectra were obtained on a Bruker 700 MHz (16.4 T) AVANCE III spectrometer using a 4 mm MAS Bruker probe. Adamantane was used as a secondary reference for ^1H and ^{13}C chemical shifts[48] whereas 85 % H_3PO_4(aq) was used as reference for ^{31}P (0.0 ppm). Due to probe signal, ^1H fast MAS NMR spectra (14 kHz) were systematically recorded using a background suppression scheme first proposed by Cory and Ritchey[49] (number of scans 8; relaxation delay 30 s for full relaxation; line

broadening 10 Hz; $t_{90°}(^1H)$ = 5.7 µs). Here, no homonuclear decoupling was applied making direct comparison with data reported in Yasar *et al*.[50] possible. The ^{13}C CP MAS NMR spectra were recorded under fast MAS (14 kHz). The precise set-up of the Hartmann-Hahn condition was performed using the 10PyACC13 and 5PyACC13 samples (90-100 ramped cross polarisation).[51] Spinal-64 ^1H decoupling (50 kHz) was applied during the acquisition (9.8 µs pulses).[52] For 10PyACC13: number of scans 5000; relaxation delay 3 s; experimental time ~ 4 h; contact time 10 ms; $t_{90°}(^1H)$ = 5.0 µs; line broadening 20 Hz. For 5PyACC13: number of scans 5000; relaxation delay 3 s; experimental time ~ 4 h; contact time 10 ms; $t_{90°}(^1H)$ = 5.2 µs; line broadening 20 Hz. The ^{13}C MAS NMR spectra were recorded under fast MAS (14 kHz) and Spinal-64 ^1H decoupling during the acquisition. For 10PyACC13: number of scans 504; relaxation delay 120 s; experimental time ~ 17 h; $t_{90°}(^{13}C)$ = 7.5 µs; 30° flip angle for quantitative measurements; line broadening 30 Hz. For 5PyACC13: number of scans 448; relaxation delay 120 s; experimental time ~ 16 h; $t_{90°}(^{13}C)$ = 8.2 µs; 30° flip angle for quantitative measurements; line broadening 30 Hz. The ^{31}P CP MAS NMR spectra were recorded under fast MAS (14 kHz). The precise set-up of the Hartmann-Hahn condition was performed using the 10PyACC13 and 5PyACC13 samples. Spinal-64 ^1H decoupling (50.0 kHz) was applied during the acquisition.[52] For 10PyACC13: number of scans 3336; relaxation delay 3 s; experimental time ~ 3 h; contact time 3 ms; $t_{90°}(^1H)$ = 5.0 µs; line broadening 100 Hz. For 5PyACC13: number of scans 10000; relaxation delay 3 s; experimental time ~ 8.3 h; contact time 3 ms; $t_{90°}(^1H)$ = 5.2 µs; line broadening 100 Hz. All simulations of spectra were performed by using the DMFit program.[53]

Results and discussion

1. Influence of the pyrophosphate amount: crystalline vs. amorphous samples

The structure of the synthesised zPyACC powders precipitated in presence of 0.0 to 10.0 mol. % of pyrophosphate in the anionic solution was characterised by XRD (Figure 1a). The powder precipitated in absence of pyrophosphate (0PyACC) showed diffraction peaks characteristics of calcite, with a maximal peak at 29.4° and apparent size of crystallites of about 112 $\pm$ 1 nm (Debye-Scherrer). This sample was not fully crystallised (87 % of crystallinity as estimated with EVA software). Calcite peaks were also present but with lower intensities in 1PyACC and 2.5PyACC XRD diagrams for which a slight contribution of a diffuse halo around 30° (more pronounced for 2.5PyACC sample than for the 1PyACC one) was detected. Indeed, the crystallinity and crystallites mean size of the 1PyACC and 2.5PyACC powders were evaluated respectively to 77 % for 70.0 $\pm$ 0.5 nm crystallites and 51 % for 57.4 $\pm$ 0.4 nm crystallites. For 3.5 % of pyrophosphate and over (*i.e.* for 3.5PyACC, 5PyACC and 10PyACC samples), only a broad halo between 25° and 35° was detected, demonstrating an amorphous structure.[54] Consequently, it appeared that adding pyrophosphate to the initial anionic solution reduced the quantity of crystalline phase of the resulting zPyACC, with a notable gap between 2.5 % and 3.5 % of pyrophosphate, leading to a fully amorphous material for initial % of pyrophosphate ≥ 3.5 %. For calcite containing materials (0PyACC, 1PyACC and 2.5PyACC), the higher the initial pyrophosphate concentration was, the smaller were the crystallites and the crystallinity.

Various domains of interest corresponding to vibrations of the carbonate and pyrophosphate groups can be detected by infrared spectroscopy (Figures 1b, 1c).[55,56] The major carbonate band constituted by a split peak at 1415 - 1490 cm^{-1} characteristic of the asymmetric stretching ν_3CO_3 of the ACC, is usually single and shifted to 1390 cm^{-1} for calcite, as in the 0PyACC spectrum. In the same way, the out-of-plane stretching ν_2CO_3 at 865 cm^{-1} for ACC is shifted to 875 cm^{-1} for calcite, and the ν_4 mode at 712 cm^{-1} for calcite is broadened and therefore not detectable for ACC. Indeed, the narrow ν_4 band of 0PyACC slowly disappeared when increasing the pyrophosphate content. In the same time, the bands

associated to pyrophosphate (δPO_3 and ρPO_3 of $P_2O_7^{4-}$ at 410 - 650 cm^{-1}, $v^{as}POP$ at 925 cm^{-1}, $v^{s}PO_3$ at 1035 cm^{-1} and the most intense band $v^{as}PO_3$ at 1070 - 1200 cm^{-1} with a maximum at 1150 cm^{-1}) and more particularly the $v^{as}PO_3$ became more and more intense (Figure 1c), showing a higher integration of pyrophosphate in the powder. Infrared and Raman spectroscopy (Figure S3) allowed identifying the PO_3 bands as similar to the ones found in pure amorphous calcium pyrophosphate.[45]

Finally, these analyses (especially the XRD) highlighted that the pyrophosphate initial content required to obtain a fully amorphous phase was between 2.5 mol. % and 3.5 mol. %. This is much higher than the low content determined by Lin and Singer[41] (0.00025 mol. %) or Sutor and Percival[57] (0.34 mol. %) but they were focusing on a delay of calcite crystallisation rather than a full inhibition of its crystallisation. On the contrary, in Ben's patent,[40] the initial pyrophosphate proportion in solution used was in the same range than in the present study, and ACC stabilised with 3.3 mol. % and 5.5 mol. % (with respect to carbonate) were still amorphous at 86 % and 96 % after 98 days in air respectively.

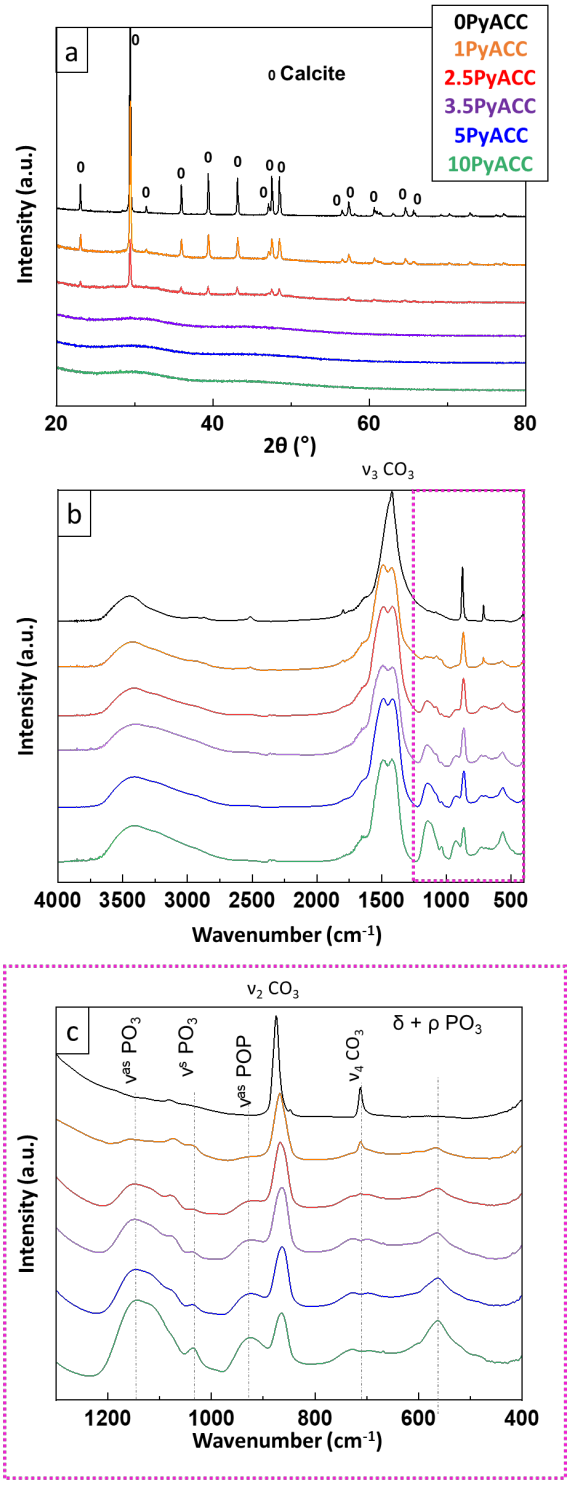

Figure 1: a) X-ray diffractograms of zPyACC powders synthesised in presence of various concentration of pyrophosphate. The narrow peaks are characteristic of calcite whereas the broad halo around 30° was attributed to the amorphous structure. b) and c) Infrared spectra of zPyACC powders with identification of the vibrational bands of carbonate and pyrophosphate groups and in c) a zoom in the 400 - 1300 cm^{-1} region (corresponding to the pink rectangle in Figure 1b).

The chemical composition of the synthesised zPyACC determined by chemical titrations (Ca^{2+}, CO_3^{2-}, $P_2O_7^{4-}$), ICP-OES (Na^+) and TGA (H_2O, Figure S4) analyses is reported in Table 1. For the 10PyACC, the pyrophosphate over carbonate ions ratio was 13.8 ± 0.5 mol. %, *i.e.* higher than the 10 mol. % introduced in the initial solution. In fact, in all of the zPyACC-synthesised powders the $P_2O_7^{4-}/CO_3^{2-}$

molar ratio was systematically higher than the initial one in solution (see first and last columns in Table 1). This was due to a competition between carbonate and pyrophosphate anions, favourable to the latter due to its higher formal charge and number of potential bonds.[41] If we consider that all of the initial pyrophosphate (5 mmol, for the 10PyACC) precipitated, 10 mmol of calcium were consumed meanwhile all of the remaining calcium (40 mmol) were associated with carbonate, leading to a theoretical Py/CO_3 ratio of 12.5% in the solid, which is in accordance with the experimental value (13.8 %). This ratio also confirmed the integration of pyrophosphate into the final powders, in agreement with FTIR spectroscopy. The calcium amount was decreasing from 0.96 mmol to 0.83 mmol for 0PyACC to 10PyACC (Table 1). The carbonate quantity showed a more pronounced decrease, from 0.96 mmol for 0PyACC to 0.64 mmol for 10PyACC in line with its unfavourable competition with pyrophosphate to be associated with calcium. The sodium amount was very low and quite constant between the different zPyACC synthesised powders, ranging from 0.00567 mmol to 0.00795 mmol. As illustrated in Figure 2, for each zPyACC sample the sum of the number of moles of calcium, sodium, carbonate and pyrophosphate ions normalised by their respective charges was lower than 0.04 mmol (for 100 mg of powder). It implied that the positive (Ca^{2+}, Na^{+}) and negative (CO_3^{2-}, $P_2O_7^{4-}$) ions charges were quite balanced, with some slight differences maybe due to a small contribution of pyrophosphate hydrolysis into orthophosphate ions (HPO_4^{2-} and/or PO_4^{3-}). Thus no other ions were integrated into the zPyACC samples in significant amounts. It was unexpected considering the high pH of synthesis (around 12) that could favour hydroxide anions integration in the solid (but no OH FTIR vibration band was observed in Figure 1b). OH^- ions were described in literature as ACC stabilisers integrated in the ACC network and an amorphous basic calcium carbonate was even mentioned in some articles, with a carbonate substitution by OH^-, enhancing thermal stability.[31,33] The presence of the pyrophosphate anions could probably explain the non-integration of hydroxide ions. The presence of hydrogencarbonate anions was prevented by the high pH synthesis as well: according to the literature, at pH 11.5 and 20°C, CO_3^{2-} ions are predominant and less than 10 % of HCO_3^- anions are observed.[58]

Table 1 : Chemical composition (Ca^{2+}, CO_3^{2-}, $P_2O_7^{4-}$, Na^+) of the synthesised zPyACC samples determined by chemical titrations and ICP-OES analysis, water content determined by TGA, and comparison of the initial $P_2O_7^{4-}/CO_3^{2-}$ molar ratio in solution (molar % introduced in the anionic solution) and the final ratio titrated in the material. Quantities are expressed in mmoles for 100 mg of powder.

	Introduced in the initial solution	**Determined by chemical titrations, ICP-OES and TGA analyses of the zPyACC powders**						
	$P_2O_7^{4-}$ / CO_3^{2-} (%)	Ca^{2+} (mmol / 100 mg)	CO_3^{2-} (mmol / 100 mg)	$P_2O_7^{4-}$ (mmol / 100 mg)	Na^+ (mmol / 100 mg)	H_2O (mmol / 100 mg)	wt.% H_2O	$P_2O_7^{4-}$ / CO_3^{2-} (%)
0PyACC	0.0 %	0.96 ± 0.09	0.96 ± 0.02	0	0.00795 ± 0.00005	0.08 ± 0.08	1.5 % ± 1.5 %	0 %
1PyACC	1.0 %	0.92 ± 0.07	0.88 ± 0.02	0.0098 ± 0.0005	0.00600 ± 0.00005	0.36 ± 0.05	6.4 % ± 0.9 %	1.11 % ± 0.03 %
2.5PyACC	2.5 %	0.88 ± 0.06	0.83 ± 0.02	0.024 ± 0.001	0.00634 ± 0.00006	0.54 ± 0.03	9.7 % ± 0.5 %	2.86 % ± 0.08 %
3.5PyACC	3.5 %	0.87 ± 0.06	0.80 ± 0.02	0.033 ± 0.002	0.00654 ± 0.00005	0.60 ± 0.01	10.8 % ± 0.3 %	4.1 % ± 0.1 %
5PyACC	5.0 %	0.87 ± 0.06	0.77 ± 0.02	0.046 ± 0.003	0.00567 ± 0.00006	0.56 ± 0.03	10.0 % ± 0.6 %	6.0 % ± 0.2 %
10PyACC	10.0 %	0.83 ± 0.06	0.64 ± 0.02	0.088 ± 0.004	0.00681 ± 0.00008	0.78 ± 0.11	14.0 % ± 2.0 %	13.8 % ± 0.5 %

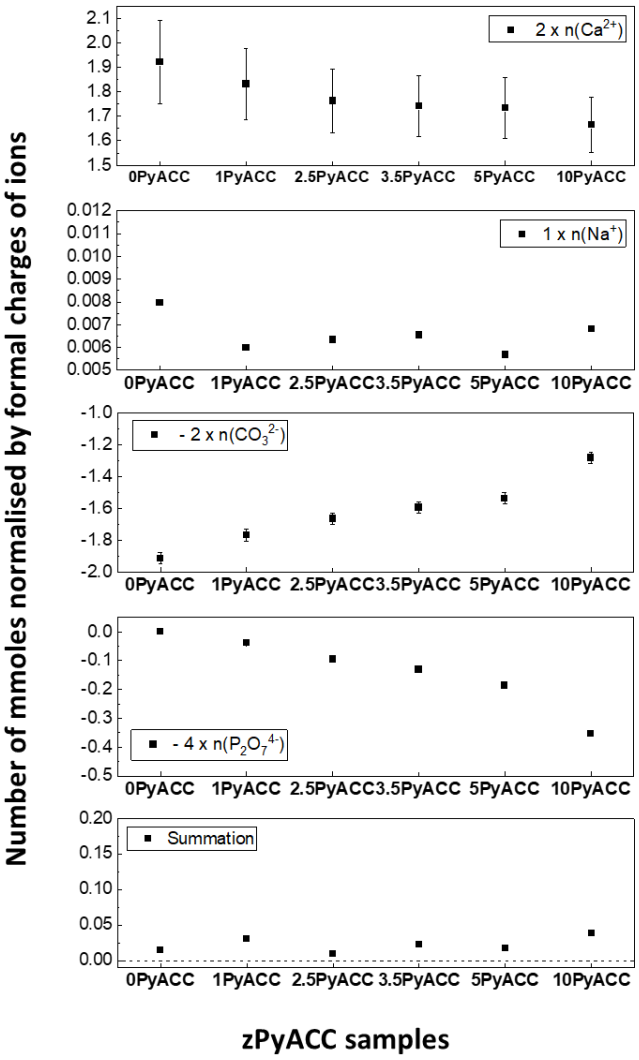

Figure 2: Number of mmoles (for 100 mg of zPyACC powder) of calcium, sodium, carbonate and pyrophosphate ions multiplied by their respective charges, in each zPyACC samples. The last graph represents the sum of the four first ones.

2. Multiscale organisation of pyrophosphate-doped calcium carbonates

FEG-SEM micrographs (Figure 3) showed the morphology of the particles of the different zPyACC samples. For the 0PyACC (Figure 3a), we obtained the typical rhombohedral calcite crystals[59] (with some little alterations or layered crystals) aggregated, which was coherent with the identification by XRD (Figure 1a). Some small globular agglomerates can also be observed (red arrow in Figure 3a, zoom in Figure 3b), characteristics of ACC which could be a transient intermediate in calcite formation.[18,22] We showed that when the pyrophosphate amount increased, more ACC was formed (Figure 1a), and a change in crystals/particles shape and size was observed (Figures 3c, 3e). Indeed, for 1PyACC, small crystals were assembled in a preferential direction along a preferential plane (anisotropy) (along the blue arrow in Figure 3c) and co-existed with rounded particles (Figure 3d), the latter being attributed to ACC.[21,37] Analogous particle morphologies can be observed for 2.5PyACC, also composed by calcite (assembled and oriented small crystals along the blue arrow on Figure 3e) and ACC (amorphous rounded particles on Figure 3f). This was in agreement with the XRD diagrams (Figure 1a) on which both sharp peaks (calcite) and a diffuse halo (ACC) can be distinguished. In addition, we could notice a decrease of the assembled crystals size from 1PyACC to 2.5PyACC sample (Figures 3c and 3e,

respectively) which was also in agreement with calcite XRD peaks widening when the pyrophosphate proportion increased in the powder (Figure 1a). As for 3.5PyACC to 10PyACC, identified as fully amorphous by XRD (Figure 1a), FEG-SEM showed agglomerates of rounded particles (Figures 3g, 3h, 3i). Measurements of a population of particles gave a diameter between 40 and 50 nm with a relative homogeneity of size.

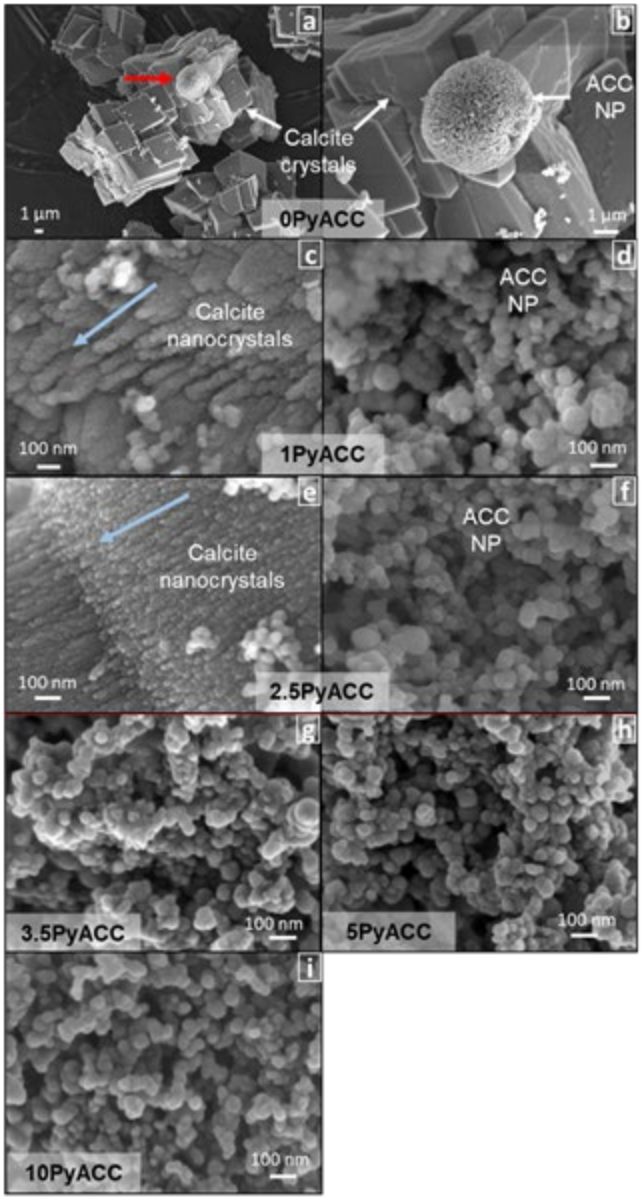

Figure 3: FEG-SEM images of the zPyACC samples synthesised with various pyrophosphate contents: 0PyACC (a and b), 1PyACC (c and d), 2.5PyACC (e and f), 3.5PyACC (g), 5PyACC (h), 10PyACC (i). The red arrow in (a) indicates where the zoom (b) was realised. The blue arrows in (c) and (e) show the preferential axis for calcite crystals growth.

The SSA was quite small (< 1 m^2/g) for 0PyACC as it was mainly composed by large calcite crystals; it increased a lot for zPyACC powders including higher proportion of pyrophosphate (Figure 4) and thus higher proportion of amorphous phase(s). Indeed, the presence of an amorphous part and the decrease of the calcite crystals size in 1PyACC and 2.5PyACC led to an increase of their SSA to 24.3 ± 0.1 m^2/g and 39.3 ± 0.2 m^2/g respectively. For the fully amorphous powders (3.5PyACC, 5PyACC and 10PyACC), the SSA was in the same range, between 47.9 ± 0.2 m^2/g and 56.6 ± 0.3 m^2/g. It was coherent regarding the FEG-SEM images and the granular shape of those particles. When compared to the

literature, it is important to ensure that the degassing parameters were equivalent whatever the samples, because they determine how much surface or structural water was removed before SSA measurements. Indeed, after preliminary tests we chose to concentrate on the removal of physisorbed water (*i.e.* 2 h of degassing at 50°C), leaving the internal/structural water because this water may be predominant for the powder structuring. The SSA measured for zPyACC powders were much lower that some reported in the literature (from 300 to 600 m^2/g) with 6 h of degassing at 100°C.[60,61] However, they were comparable to the SSA of 42 m^2/g for a 50 nm-ACC (degassed 18 h at room temperature)[62] or of 42 m^2/g for 90 nm-ACC (without degassing).[63] The SSA of 0PyACC was also similar to the 0.99 m^2/g of calcite (degassed 18 h at room temperature).[62] By FEG-SEM (Figures 3g, 3h, 3i) we observed similar particles sizes for the fully amorphous zPyACC samples. However, the SSA being dependent of the size of particles, we expected smaller nanoparticles when increasing pyrophosphate content but this cannot be discernible due to the limit of resolution. DTA (Figure S5) showed an increase of the crystallisation temperature (first exothermic peak[30]) when increasing the pyrophosphate content, which goes from 362°C for 5PyACC to 432°C for 10PyACC. This is in line with the decrease of the particle size[64] and a higher stability regarding crystallisation, as it was already shown for orthophosphate-stabilised ACC.[14,37] The second exothermic peak, clearly noticeable for 5PyACC and 10PyACC, may be related to the internal hydrolysis of pyrophosphate into orthophosphate involving structural water, and its crystallisation into hydroxyapatite.[56] An endothermic peak around 110°C was present in the thermograms of all the zPyACC samples, associated to the loss of adsorbed and structural water.

A smaller particle size with higher pyrophosphate contents let us assume that Py had a surfactant role or in other words a complexing role (as clusters could be assimilated as big macromolecules). Additives decreasing the particles size are indeed documented and relatively common for various types of compounds, and in particular for phosphates,[14,37] increasing stability toward temperature. It was also observed for pyrophosphate additives in one study.[38]

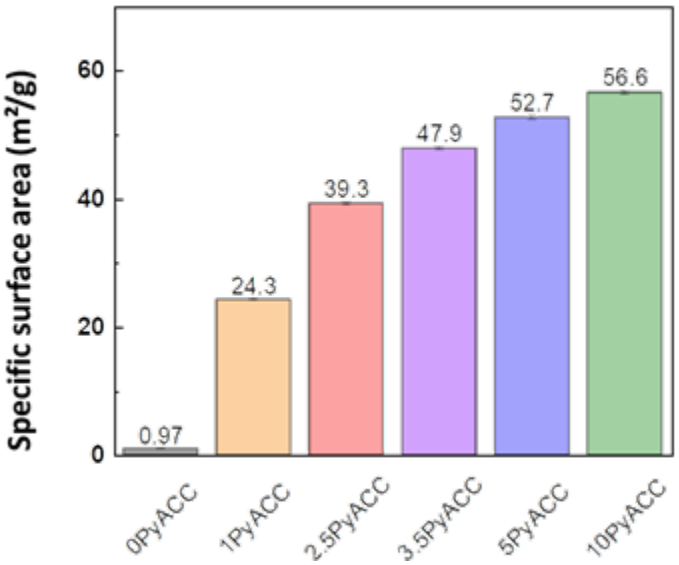

Figure 4: Specific surface area of the synthesised zPyACC powders, measured by the BET method.

STEM observations of 5PyACC (Figure 5) and 10PyACC (data not shown) were realised after resin inclusion and ultramicrotomy. Almost spherical particles of various sizes, with diameters ranging from 10 to 60 nm for 10PyACC and 70 to 100 nm for 5PyACC, were observed. The particles analysed were smaller in the 10PyACC cross section than in the 5PyACC's one and less particles are present in the

latter. As larger particles were removed from the cross section during cutting, these observations could be related to the surfactant role of pyrophosphate discussed earlier, stabilising more numerous and smaller particles (as observed for 10PyACC compared to 5PyACC). The particles were amorphous but some parts quickly crystallise under the electron beam, as attested by fast Fourier Transform of the STEM images (not presented here). The dark field TEM image in Figure 5 (where heavier elements appeared in lighter colour) showed that the 5PyACC nanoparticles seemed quite homogeneous in term of elemental distribution at the beginning of the observation (Figure 5a). However, a zone of lower electronic density quickly appeared (Figure 5b) and grew under the beam (Figure 5c) during the EDS analysis, but without modifying the external shape of the particle, as it could be seen in the movie in Supporting Information (SI-F). We could attribute this phenomenon to the water radiolysis, identified by Du *et al.*:[65] structural water transformed into water vapour due to the beam energy, then was entrapped into the particle by the surrounding resin barrier, forming a bubble inside the particle. A correlation between the number of bubbles and the water content was established by these authors, but not observed in the present study due to the small particles size and the small number of zPyACC samples analysed (only two). Furthermore, EDS analyses highlighted the homogeneous distribution of oxygen, phosphorus and calcium in the volume, suggesting a homogeneous coexistence of carbonate and pyrophosphate units at the nanoscopic scale (see more explanations in Supporting Note SI-F). This elemental repartition and water radiolysis were also observed for the other particles analysed from these two samples.

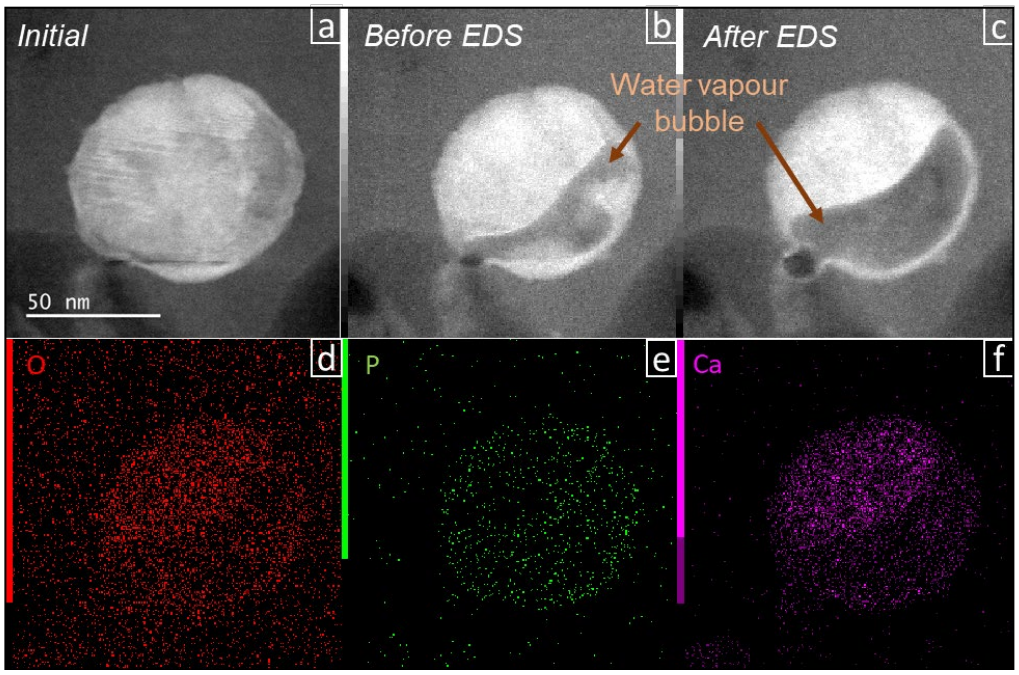

Figure 5: 5PyACC STEM images, after inclusion in resin and ultramicrotomy. Dark field images taken just after focalisation (a), and before (b) and after (c) EDS analysis. The water vapour bubble formed by radiolysis was identified by the red arrows on (b) and (c) The oxygen (d), phosphorus (e) and calcium (f) elemental distributions were evaluated for a 60 frames (6min34s) EDS mapping. Oxygen also appears outside of the particle as a constituent of the polymeric resin.

The SAXS plotting in Figure 6 showed a different behaviour between the crystalline powders (0PyACC and 1PyACC) and the other ones. Indeed, the intensity was increased for the 2.5PyACC to the 10PyACC, corresponding to an increase of the electronic density and so on of a densification of the powders. It could appear counterintuitive regarding the FEG-SEM images in Figure 3, where the powders appeared fractals from the 2.5PyACC to the 10PyACC. However, there was some free space between the large

crystals present in the 0PyACC and 1PyACC samples, not present into the other powders with aggregated nanoparticles. Consequently, the latter were denser.

Beyond this general trend, the SAXS curves can be divided in four domains,[66] as illustrated in Figure 6:

- small scattering vector q (domain I), giving at the slope change a first dimension D_1 characteristic of the nanoparticles size;
- the slope giving information on the surface of the nanoparticles (domain II);
- intermediate q (domain III), representative of an intra-particles size R_2 and internal interactions;
- finally, larger q (domain IV) corresponding to scattering/diffraction induced by the atomic network and crystal lattice if any.

By fitting with a power law at small scattering vectors both of the slopes before and after the inflexion point, the SASView software allowed determining the first dimension D_1 of the nanoparticles, listed in Table 2. Briefly, the power law is defined by the expression $I(q) = k.q^{-p}$, where k and p can be obtained by the fit. Then, the intersection point of both lines corresponds to $q_1 = 2\pi/D_1$. The size of the nanoparticles was significantly decreased when increasing the pyrophosphate amount, from 104.0 $\pm$ 1.0 nm for 1PyACC to 51.9 $\pm$ 0.2 nm for 10PyACC. Nevertheless, this diameter had only slight variations with the pyrophosphate amount for fully amorphous samples (between 59.3 $\pm$ 0.4 nm for 3.5PyACC and 51.9 $\pm$ 0.2 nm for 10PyACC). These results were in good agreement with FEG-SEM results and reinforced the hypothesis of surfactant properties of pyrophosphate highlighted by the latter technique. It was confirmed by the slope (between 3.9 and 4.0) of the intermediate part of the curve (see domain II, Figure 6), synonym of a defined surface that can be correlated to smooth particles surfaces observed with FEG-SEM. The difference between the crystallite size calculated through the Scherrer formula based on the XRD data (Figure 1a) and the values obtained here from SAXS data were not discussed here. Considering pure ACC, the average diameter described in the literature varies between 0.7 nm and 200 nm. Indeed, a population of small (0.7 nm - 1.1 nm) ACC particles was mentioned, co-existing with bigger ones (30 nm - 250 nm).[67] Nanoparticles of 20 nm - 50 nm were often obtained,[17,19,21] sometimes assembled in a secondary nucleation step in 60 nm - 120 nm particles[19,68] or gathered in 50 nm - 100 nm aggregates.[21] Some bigger ACC particles (up to 200 nm[64]) were seen by SEM, but possibly being agglomerates. Hence, in the present study we are in line with most published articles.

Going to higher q (domain III in Figure 6), a maximum of intensity (small hump) was observed around 0.17 $Å^{-1}$ for all the curves apart for the 0PyACC one. With the approximation of a spherical shape for the intra-particles entities, assuming they were constituted of calcite or vaterite core (based on proto-calcite or proto-vaterite clusters as detailed in the introduction[21] and considering that calcite or vaterite were the inhibited crystalline phase) into an aqueous environment, a sphere model with a structure factor S(q) (hard sphere model) was used to determine their size (see Supporting Note SI-G for more details and Figure S6). It appeared that all of the powders from 1PyACC to 10PyACC contained small entities of the same radius of 2.5 nm. Hence, these 5 nm-diameter entities would be characteristic of this pyrophosphate-stabilised ACC, no matters the Py quantity.

Looking at larger scattering vectors than for the X-rays scattering, the WAXS 2D curves were obtained (Figure 7a), with diffraction peaks for the 0PyACC, 1PyACC, 2.5PyACC as well as small ones for the 3.5PyACC. Whereas for the first three powders the conventional X-rays diffractograms (Figure 1a) already indicated the presence of calcite crystals, for the latter (3.5PyACC) they were observed only with this wide-angle technique, probably due to a longer counting time on each angle. In the zoom in Figure 7b showing the peaks region with shifted curves (for more clarity), the peaks of 0PyACC and some of 1PyACC and 2.5PyACC could be identified as calcite ones (grey lines). However, other peaks,

with a relative intensity higher in the 1PyACC and 2.5PyACC rather than in the 0PyACC (without pyrophosphate), could be attributed to vaterite (pink lines). Their presence could be due to the calcite inhibitor role of pyrophosphate, which quantity was too small to fully inhibit crystallisation but which partially prevented calcite formation, leaving some possibilities for vaterite precursor to form.

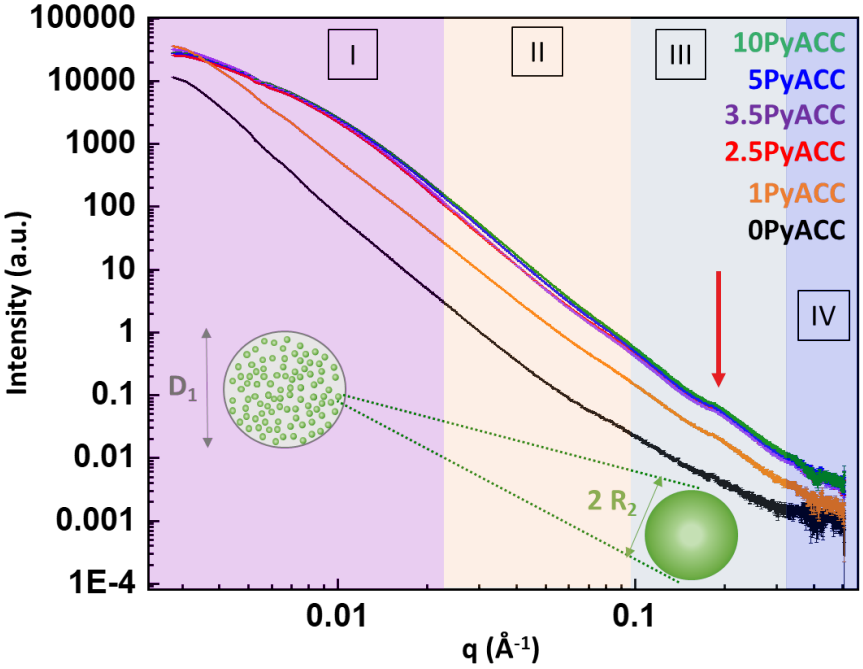

Figure 6: Experimental SAXS data of the zPyACC samples, plotted as log(I(q))=log(q), with I the intensity and q the scattering vector. Four domains can be identified. The first curvature around q = 0.07 Å^{-1} in the domain I gave us information about the size of the nanoparticles D_1, the slope of the line in domain II about the surface of the nanoparticles; meanwhile the hump around q = 0.2 Å^{-1} in domain III, highlighted by the red arrow, and present for all except the 0PyACC, was attributed to the entities with a radius R_2.

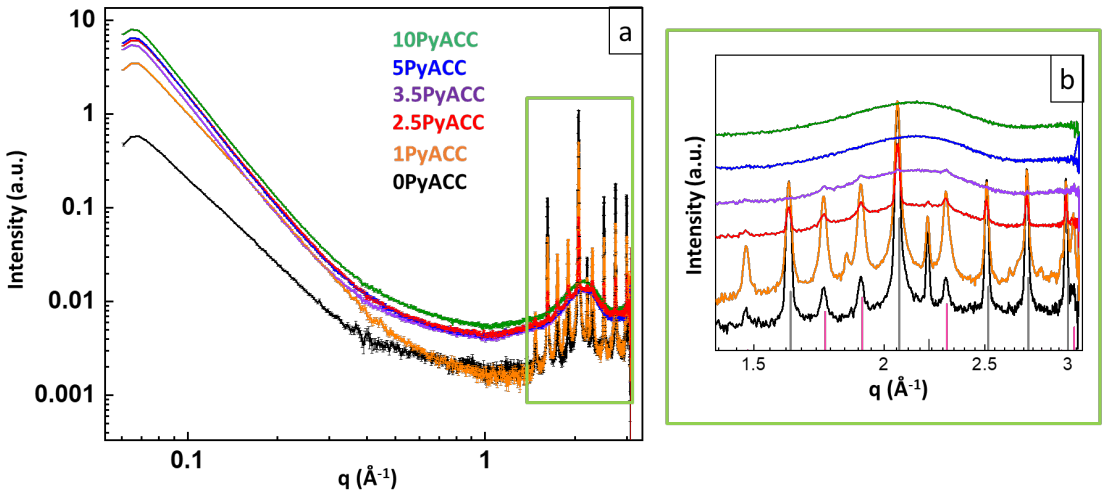

Figure 7: Experimental WAXS2D data (a) and zoom in the green rectangle (b) of the zPyACC, plotted as log(I(q))=log(q), with

I the intensity and q the scattering vector. The zoom (b) presents the curves with a shift for better clarity. The grey and pink bars correspond respectively to the calcite and vaterite calculated pattern (from the XRD JCPDS database).

Table 2: Diameter of the nanoparticles D_1 and radius of the intra-particles entities R_2 for the zPyACC powders. It was not determined for the 0PyACC because the sphere model used for the fitting was not consistent with the cubic calcite crystal shape observed by FEG-SEM (Figures 3a and 3b). The uncertainties are coming from the fitting process.

	D_1 (nm)	R_2 (nm)
1PyACC	104.0 ± 1.0	2.48 ± 0.02
2.5PyACC	66.3 ± 0.4	2.482 ± 0.008
3.5PyACC	59.3 ± 0.4	2.478 ± 0.008
5PyACC	54.4 ± 0.3	2.461 ± 0.008
10PyACC	51.9 ± 0.2	2.485 ± 0.008

3. Toward a pyrophosphate-stabilised ACC model

To further investigate the structuration of the amorphous phase and its potential evolution in this series of zPyACC samples, PDF analysis was performed for all the samples. Briefly, the pair distribution function, G(r), describes the probability of finding a pair of atoms at an r distance (see SI-H1 for more details).[69–71]

Figure 8 clearly showed that 1PyACC and 2.5PyACC powders were crystalline (as expected from XRD) whereas the 3.5PyACC, 5PyACC and 10PyACC powders were amorphous (coherence length, *i.e.* the maximum distance in the powder for which the atoms are organised < 10 Å). Crystalline samples, Figure S8 and Table S1, showed coherence length above 50 nm, 52-58 nm for 1PyACC and 50-55 nm for 2.5PyACC, knowing that at such high distances, specific values are difficult to determine by PDF curves. It was interesting to note that both coherence lengths were close, but the peak intensities tended to decline with r much faster for 2.5PyACC than for 1PyACC, giving insight of a possible additional phase. As expected from XRD, both experimental 1PyACC and 2.5PyACC PDF curves only presented peaks at distances corresponding to calcite.[72] Given the different intensity attenuations between reference calcite, 1PyACC and 2.5PyACC, intensity normalisation had been imposed based on a high r peaks. It showed that all samples presented the same structure at high distances, *i.e.* calcite, but that an additional amorphous phase was also present at small order (below 9 Å). Subtraction between experimental pure calcite curve and either 1PyACC or 2.5PyACC experimental curves allowed us to confirm the presence of additional amorphous phase, and to attest that this amorphous phase was similar for both samples (called a1PyACC and a2.5PyACC). Its proportion was getting higher with higher amount of pyrophosphate (Figure S10c). In addition, Figure 9a also proved that a1PyACC and a2.5PyACC presented the same organisation as 3.5PyACC, 5PyACC and 10PyACC. Figure S11 indicated that this amorphous phase clearly had a different structuration than calculated amorphous calcite (calcite pattern with an imposed signal attenuation at 8 Å (see Supporting Note SI-H3 for more details), but, as seen in Figure 9b, was close to amorphous vaterite (calculated on the basis of Demichelis's representation[73] and likewise artificially attenuated at 8 Å). All in all our results showed that starting from reference calcite (0PyACC) synthesis, the presence of pyrophosphate during the co-precipitation decreased the amount of calcite, and produced an increasing amount of proto-vaterite amorphous

phase. Above 3.5 % Py, the sample was composed with only this proto-vaterite amorphous phase, as described by Gebauer *et al.*[21] Synthetic and biogenic ACC mainly display an organisation at a short or medium-range of about 8-10 Å, as proven by PDF[14,74,75] or EXAFS spectroscopy.[6] At this short distance order, some ACC structures were shown to present the same organisation as one of the $CaCO_3$ crystalline phase. Indeed, similarities to calcite structure were demonstrated by NMR,[21,22] FTIR spectroscopy,[21,22] EXAFS[22,26] and PDF:[24] this ACC was called proto-calcite ACC. In the same way, proto-vaterite (NMR,[21] FTIR,[21] and EXAFS[27] spectroscopies) and proto-aragonite structures (NMR,[23] EXAFS,[23,27] PDF[25]) were also observed in synthetic ACCs. Yet, the similarities to a known-crystalline polymorph were subtle, and some articles described a short-range organisation that differed from all of the known crystalline forms[14,75] or no short-range organisation at all (maybe due to a synthesis at high supersaturation).[76] Proto-crystalline structures were also identified for biogenic ACC, either as proto-calcite in Ficus cystoliths (EXAFS spectroscopy),[35] in sea urchin embryos (EXAFS spectroscopy)[77] or in avian eggshell (FTIR spectroscopy)[78] or as proto-aragonite in the shell of freshwater snails (EXAFS spectroscopy).[79] In the present study the obtaining of a proto-crystalline structure was expected, and the similarities to the vaterite phase were not surprising taking into account the known calcite inhibition properties of pyrophosphate ions.

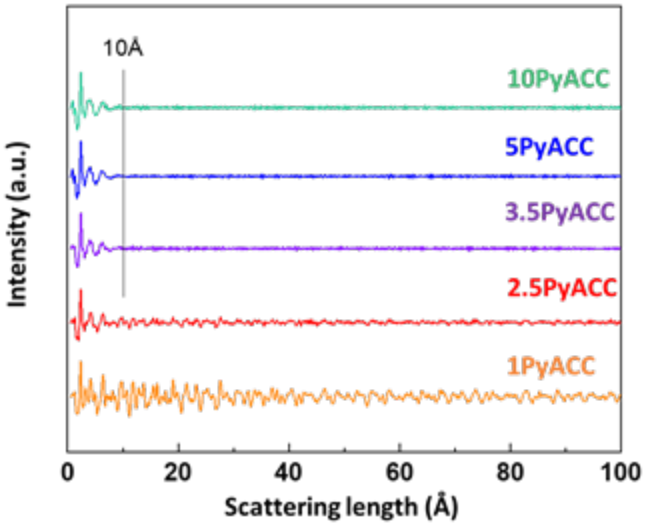

Figure 8: Experimental PDF curves (Gexp(r)) of the zPyACC synthesised samples, with the 10 Å length highlighted.

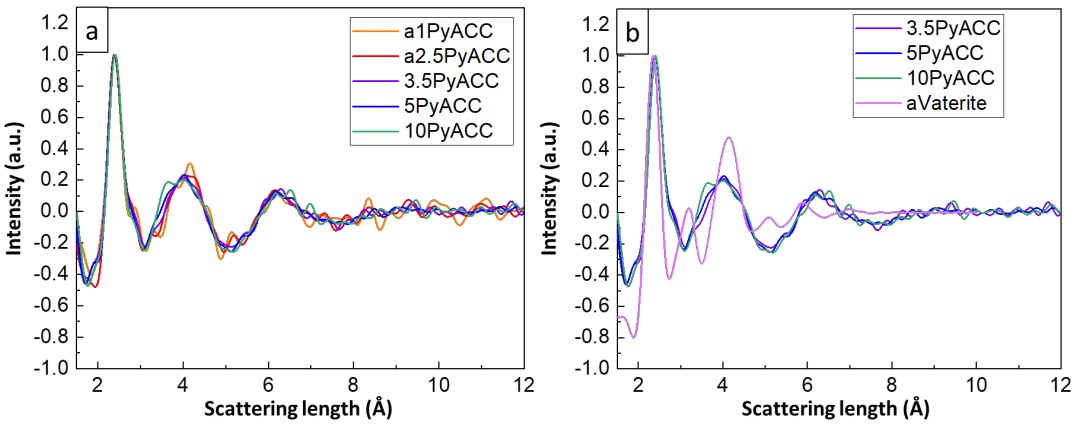

Figure 9: PDF comparisons of the amorphous phase of the 1PyACC and 2.5PyACC (a1PyACC and a2.5PyACC respectively, see details in the Supporting Note SI-H4) with 3.5PyACC, 5PyACC and 10PyACC Gexp(r) (a). Comparison of experimental 3.5PyACC, 5PyACC and 10PyACC PDF curves with the calculated "amorphous" vaterite (aVaterite) (b) (see details on the calculation in the Supporting Note SI-H3).

In order to unravel the localisation of each constitutive ion and to build a model of the PyACC clusters, solid-state NMR was performed on the 5PyACC13 and 10PyACC13 powders. The ^{1}H MAS NMR spectra of 10PyACC13 and 5PyACC13 are presented in Figure 10. Despite limited resolution and following Yasar *et al.* in the case of amorphous calcium phosphate phases doped with carbonate,[50] three regions could be observed corresponding to the following values of $\delta_{iso}(^{1}H)$: ~ 5.0 ppm, ~ 7.0 ppm (as a shoulder) and a broader (and very minor) range located at [10 ppm-13 ppm]. Such contributions were observed as well in the case of amorphous calcium pyrophosphates.[80] Yasar *et al.*[50] assigned the resonance at ~ 5.0 ppm to loosely bound (physisorbed) water molecules and a resonance at ~ 7.0 ppm to strongly bound molecules. From 5PyACC13 to 10PyACC13, one saw no clear modification on the ^{1}H NMR spectra. This indicated that the "loosely" bound water molecules were not particularly sensitive to the increase in pyrophosphate species, at these %. The presence of the shoulder at ~ 7.0 ppm in both samples supported the idea of a strongly bound "pseudo-structural" water in addition to the surface adsorbed one, highlighted by TGA curves (Figure S4) with a mass loss associated to dehydration occurring until almost 300°C.[74] However, this amount was really small compared to the free water, as the shoulder was much less pronounced than in Yasar's ^{1}H MAS NMR spectra.[50] The resonances in the [10 ppm - 17 ppm] region may be assigned to HPO_4^{2-} or HCO_3^- species but in a very low amount.

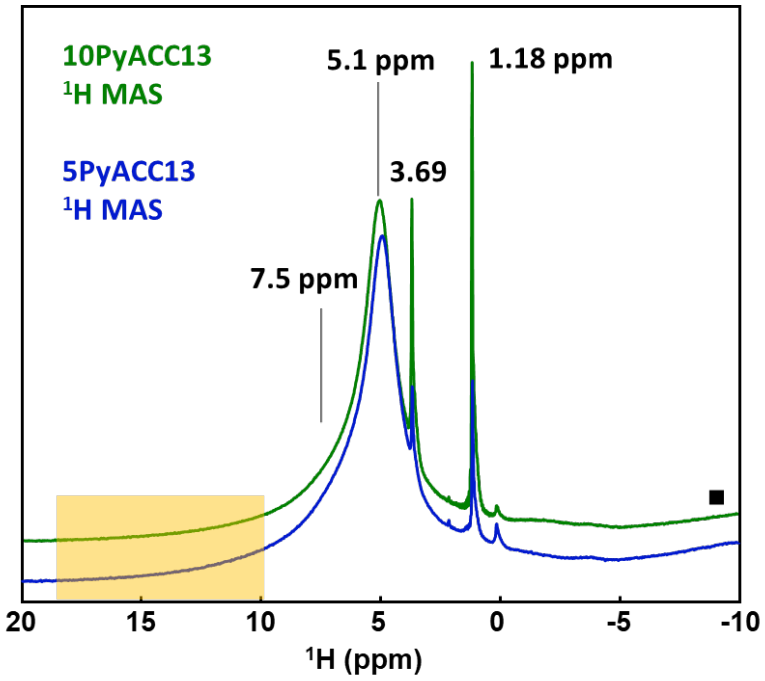

Figure 10: ^{1}H MAS NMR spectra of 10PyACC13 (in green) and 5PyACC13 (in blue). The very sharp lines at 3.69 and 1.18 ppm correspond to minor ethanol impurity. ■: residual background signal. The orange rectangle corresponds to the resonances of acidic phosphate groups (if present), following Yasar et al.[50]

In addition, for both samples, ^{13}C MAS and CP MAS NMR spectra were not exactly superimposed but the difference did not exceed the limit of ± 0.04 ppm (Figures 11a, 11b) which could be related to instrumental drifts. This demonstrated that the global distribution of water molecules can be considered as homogeneous regarding the carbonate, *i.e.* there is no important water-free area within the powders (as can be obtained with micro-sized anhydrous crystals for instance). Indeed, 5PyACC and 10PyACC contained important amount of water (evaluated with TGA, Table 1), up to 0.78 mmol (for 100 mg of powder) for 10PyACC (14.0 wt. %), this amount decreasing significantly with the pyrophosphate one, as 0PyACC, mainly composed by calcite, contained only 0.08 mmol of H_2O (equivalent to 1.5 wt. %). This is in line with most of the synthetic ACC described in published articles, containing between 11 and 22 wt.% water (*i.e.* from 0.7 to 1.6 mole of water for one mole of carbonate),[14,37,75] and even with the stable biogenic ones (approximatively 15 wt. % of structural water[6,35]). Water is described as an ACC stabiliser, by preventing carbonate re-organisation and dehydration with hydrogen bonds.[28,81] Consequently, the thermodynamic stability of ACC increases with its hydration state; the increase in water content we showed in zPyACC samples when pyrophosphate content increased reinforced this hypothesis.

The ^{13}C CP MAS NMR spectra of 10PyACC13 and 5PyACC13 samples are presented in Figures S12a, S12b, respectively. Here, the whole spectra were shown in order to highlight the major CO_3^{2-} contributions and the (very) small HCO_3^- contributions (vertical blue arrows).[50] Such contributions were observed only on the ^{13}C CP MAS spectra and were almost non-detectable in the corresponding ^{13}C MAS NMR spectra (Figures 11a, 11b). The simulation of the ^{13}C MAS and CP MAS NMR spectra (Figures 11a, 11b) was straightforward using two components, one being of very minor intensity (HCO_3^-). The parameters, in Table 3, corresponded to those of optimised in DMFit software.[53] The isotropic chemical shift distribution for the CO_3^{2-} was estimated to a line width (LW) of 3.56 ppm, in full agreement with data reported by Yasar et al.[50] HCO_3^- species exhibited a larger isotropic chemical shift distribution (LW = 5.72 ppm). Such values are in full agreement with data already reported in the literature.[21,50,82] More specifically, $\delta_{iso}(^{13}C)$ = 168.42/168.47 ppm were close to the values observed for proto-calcite (pc) or proto-vaterite (pv)-ACC, 168.7 ppm and 169.5 ppm respectively.[21] Most

importantly, the ^{13}C MAS and CP MAS spectra obtained under fast MAS (14 kHz) for 5PyACC13 and 10PyACC13 were not subjected to any variations in time. It is in strong contrast with data reported by Gebauer *et al.*[21] showing a clear evolution of the spectra from ACCs to more crystalline calcite and vaterite phases (such transformations could be associated to centrifugal forces in the rotor and/or local heating due to air friction). It highlighted the net effect of Py moieties as a factor of stabilisation for 5PyACC13 and 10PyACC13. Such moieties could be tightly bound to carbonate proto-crystalline clusters and water molecules through H-bonds. As the number of carbonate molecules *per* proto-crystalline cluster is small (approximatively 17 carbonates ions *per* cluster, as calculated considering the number of carbonates *per* vaterite cell, the volume of the cell and the volume of the 1 nm-cluster), the effect of closely located Py on $\delta_{iso}(^{13}C)$ could be noticeable. In other words, the observed centre of gravity of the resonances located at $\delta_{iso}(^{13}C)$ = 168.42/168.47 ppm could be associated to proto-crystalline clusters bound to Py molecules (in ref.[21], proto-calcite (pc) or proto-vaterite (pv)-ACC reported at $\delta_{iso}(^{13}C)$ = 168.7 and 169.5 ppm corresponded to samples obtained in the absence of additives). In this case, the ^{13}C chemical shifts associated to crystalline calcite and vaterite were not suitable for direct assignment of the proto-phases.[21] The pc *vs* pv nature of the ACC was given by PDF analyses (see above, Figure 9b) and not by solid state NMR solely.

The ^{31}P CP MAS NMR spectra of 10PyACC13 and 5PyACC13 are presented in Figures 11c and 11d, and the quantitative values are presented in Table 3. Each spectrum exhibited a major component assigned to pyrophosphate species (~ -6.7 ppm), and with several associated spinning side bands.[80] A minor deshielded component was observed as well ($\sim$ 2.9 ppm). Gras *et al.*[80] and Slater *et al.*[83] assigned this particular component to traces of orthophosphates, respectively 8.6 % and 8.8 % for 5PyACC13 and 10PyACC13. They can result from the partial hydrolysis of pyrophosphate ions under ageing,[56] being consistent with the differences to the charge balance observed in the sum of the ions amounts in Figure 2. The characteristics of the orthophosphate resonances (Table 3) were in very close agreement with those observed for carbonate doped amorphous calcium phosphate phases.[50] ^{31}P CP MAS NMR yet confirmed the integration of pyrophosphate into the resulting material. Even though the $P_2O_7^{4-}$ peak position (δ_{iso}) of 5PyACC13 and 10PyACC13 were close (respectively – 6.6 ppm and – 6.8 ppm), their width at half maximum (LW) differed (6.9 ppm and 7.2 ppm respectively). It may be due to a different environment of Py ions. Indeed, pyrophosphate anions can bond to the calcium carbonate core through H-bonds from the water molecules, stabilising the proto-vaterite structure. At a higher Py amount, when all of the clusters are stabilised the remaining Py anions could be located close to the surface of the larger nanoparticles and act as surfactants, reducing their size (as illustrated by SAXS and BET analyses – see section 2 above) and leading to the broadening the corresponding ^{31}P resonance.

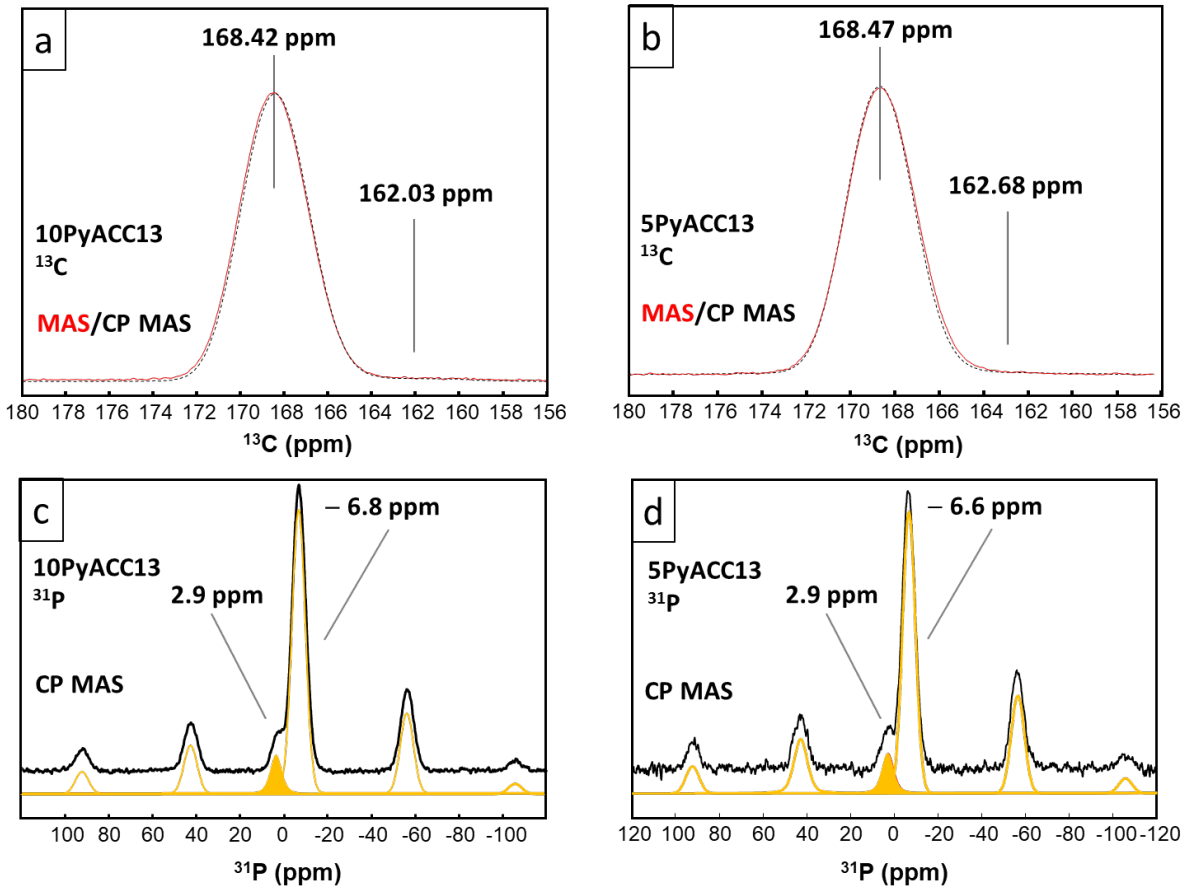

*Figure 11: ^{13}C CP MAS (black dashed) and MAS (red) spectra of 10PyACC13 **(a)** and 5PyACC13 **(b)**. Vertical lines indicate the resonances of CO_3^{2-} and HCO_3^- (see also Figures S12a, S12b). ^{31}P CP MAS spectra of 10PyACC13 **(c)** and 5PyACC13 **(d)**. Orange, plain: PO_4^{3-} and/or HPO_4^{2-} species. Orange: $P_2O_7^{4-}$. The corresponding isotropic $\delta_{iso}(^{31}P)$ ranges are indicated. The other resonances correspond to spinning sidebands (mostly from $P_2O_7^{4-}$ species).*

Table 3: Parameters of the ^{13}C CP MAS and ^{31}P CP MAS NMR spectra of 5PyACC13 and 10PyACC13 samples, considering the main resonance of CO_3^{2-} and $P_2O_7^{4-}$ respectively but also the minor ones (HCO_3^- and $PO_4^{3-}$and/or HPO_4^{2-}).

	Sample	δ (ppm)	LW (ppm)	xG/(1-x)L	%
CO_3^{2-}	5PyACC13	168.47	3.56	1.00	
	10PyACC13	168.42	3.56	1.00	
HCO_3^-	5PyACC13	162.68	5.72	0.98	< 1.0 %
	10PyACC13	162.03	5.72	0.98	< 1.5 %
$P_2O_7^{4-}$	5PyACC13	- 6.6	6.9	1.00	
	10PyACC13	- 6.8	7.2	1.00	
PO_4^{3-} and/or HPO_4^{2-}	5PyACC13	2.9	6.2	0.50	8.6 %
	10PyACC13	2.9	6.1	0.47	8.8 %

Taking into account all of the multiscale advanced characterisation results, a model of the PyACC nanoscale cluster was build, presented in Figure 12. PDF analyses highlighted the existence of a 1 nm-proto-vaterite cluster (in grey in Figure 12), including exclusively Ca^{2+} and CO_3^{2-} entities organised similarly to the vaterite crystal structure. It is in line with theoretical studies from Colas *et al.*[68] stating

the existence of some ordered anhydrous $CaCO_3$ clusters surrounded by highly hydrated regions, as demonstrated by Monte-Carlo simulation and PDF on Mg-doped ACC. In our case, pyrophosphate anions may surround the proto-vaterite cluster being tightly linked through H-bonds from the water molecules as highlighted by solid-state NMR, probably stabilising it since its early formation during precipitation (cf. PNC theories developed in the introduction), in agreement with their calcite crystallisation inhibiting role described in the literature.[41] When the Py amount is too low, they do not allow stabilising all the pre-nucleation clusters and consequently some of them could lead to crystal nucleation (*i.e.* dehydration and ordered aggregation of PNCs) and subsequent growth of crystals. Around 3.5 % of Py/CO_3, all of the PNCs are probably stabilised by pyrophosphate anions surrounding them, and the remaining Py start to stabilise the ACC nanoparticles (in light blue in Figure 12) as well (explaining the increase of SSA (Figure 4), the decrease of particles size (Table 2) and the $P_2O_7^{4-}$ peak (δ_{iso}) broadening (Figures 11c, 11d)). There is an apparent contradiction with the study of Kababya *et al.,* describing by solid-state NMR an amorphous calcium carbonate phosphate phase (ACCP).[84] Indeed, the latter consists in a homogeneous dispersion of phosphates through the ACC matrix but at a nanoscale (each carbonate has a phosphate in its 9 Å sphere). Nonetheless, at this 1 nm-scale in our model, every phosphate is in the vicinity of a carbonate, appearing as homogeneously dispersed too. Our study could also be consistent with the results of other articles on phosphate-stabilised ACC.[38,85] A denser but thin layer of "pseudo-structural" water, highlighted by TGA-DTA and ^1H NMR, would be in close vicinity of proto-vaterite and strongly linked to the Py units, avoiding ACC dehydration and so its re-organisation and crystallisation, as for phosphates.[84] Pyrophosphates could also avoid the crystallisation by strong electrostatic interactions between pyrophosphate and calcium from the proto-vaterite clusters. The 2 nm-outer layer surrounding the PyACC cluster would consist in mobile water and the remaining calcium ions (as illustrated by the chemical titrations in Table 1). Even if calcium-pyrophosphate ion-pair formation is favoured compared to the calcium-carbonate one (as previously seen), we can assume that these Ca-Py ion pairs stabilise the proto-vaterite clusters instead of forming pure CaPy clusters and subsequently crystallise as calcium pyrophosphate. Indeed, we did not detect any evidence of the presence of Ca-Py entities (clusters) at a nanoscale. A recent study of Clark *et al.* [86] revealed the same kind of model for undoped ACC based on neutrons and x-ray scattering combined to reverse Monte Carlo modelling, with 55 nm-ACC particles containing crystalline anhydrous nanodomains of 2 nm which cohesion relied on interstitial strongly bound water molecules. Moreover, molecular dynamics simulation assessed the stability of such organisation, in particular when in contact with a water interface.

To summarise, the effects of pyrophosphate on obtaining ACC are the following:

i) Py ions reduce the size of the crystals if any and allow the formation of an amorphous phase;
ii) Py ions favour and stabilise the proto-vaterite cluster, maybe through hydrogen bonds from water molecules to carbonate ions, and subsequently avoid the crystallisation;
iii) When all of the proto-crystalline clusters are stabilised, Py anions act as surfactants and reduce the nanoparticles size;

The increase of the Py amount is somehow related to the one of water into PyACC powders.

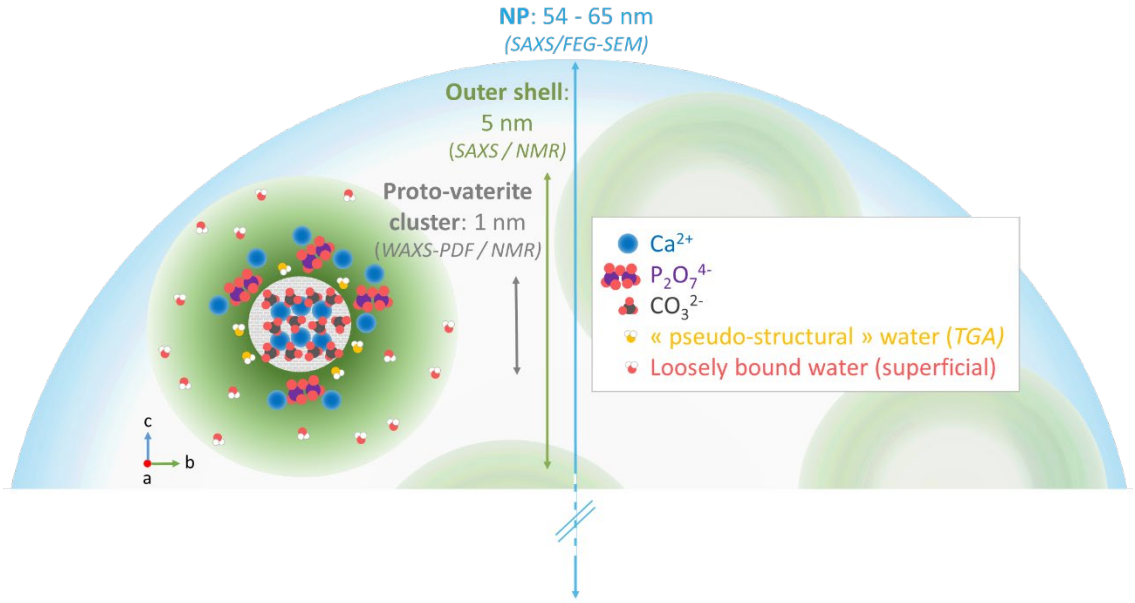

Figure 12: Schematic representation of the PyACC cluster model based on the complementary data from the advanced characterisation techniques implemented.

Conclusion

The effects of pyrophosphate ions on the multiscale structure and composition of ACC precipitated in their presence have been thoroughly described from the nanoscale to the macroscopic level through complementary advanced techniques. For a Py/CO_3 ratio lower than 3.5%, the pyrophosphate reduces the size of the calcite crystals and allows obtaining an additional phase of ACC, in an increasing amount for higher Py. We demonstrated that the latter is organised in the same way as in the fully amorphous PyACC, and contains a 5 nm-diameter intra-particle entity, in which the 1 nm-core is organised similarly to vaterite (and so called proto-vaterite cluster). The pyrophosphate is in close vicinity to this vaterite-like organised core and stabilises it. Indeed, when the Py amount is too low, some clusters start aggregating and dehydrating, leading to calcite crystals nucleation and growth. However, when all of the clusters are stabilised and a fully amorphous compound is obtained, pyrophosphate ions may act as surfactants stabilising the whole 50 – 60 nm ACC nanoparticles, reducing their size. We showed that small amounts of orthophosphates and negligible amounts of other ions (hydrogencarbonate, hydroxide ions) are included into this amorphous phase, but that water is in an increasing amount when the Py quantity increases. A small part of the water is strongly bound to the proto-vaterite cluster and the Py units (pseudo-structural water) and has an important role for stabilising the amorphous phase. The other remaining water (major part) is more labile and distributed homogeneously in the outer layer and/or adsorbed to the surface of the PyACC nanoparticles. The model proposed here, consistent with all of the multiscale complementary characterisation results we obtained and most of the literature, is of huge interest, as additives-stabilised ACC were poorly described in term of nanoscale structure. It is a predominant prerequisite to understand the underlying mechanisms of the formation, evolution or dissolution of ACC. Indeed, such comprehensive study could highlight the correlation between the nanostructure evolution, the release kinetic and finally the biological properties of zPyACC materials. From our point of view, these results and the associated methodology pave the way to the rational design of tunable amorphous and bioinspired inorganic biomaterials for bone applications.

Conflicts of interest

There are no conflicts of interest to declare.

Acknowledgements

The authors thank the Raymond Castaing Microcaracterisation centre, and in particular Alessandro Pugliara and Teresa Hungria for TEM analyses and Stéphane Le Blond du Plouy for FEG-SEM analyses. The French FERMaT Federation FR3089 is acknowledged for providing SAXS laboratory facility.

Funding

The authors thank the Occitanie Region (BioPhORM project n°19008740/ALDOCT-000734) for supporting this research work.

Author contributions

MM and CR set the synthesis protocol for PyACC powders. MM carried out the synthesis of all the zPyACC samples and their physico-chemical analyses. Among the advanced characterisation PR carried out the SAXS experiments, CS the WAXS-PDF analyses and CB the solid state NMR analyses. CC and JS supervised MM research work and CC secured funding. MM mainly wrote the initial draft of the manuscript, and all authors contributed to the final version of the article.

Bibliography

1 A. Lucas, J. Gaudé, C. Carel, J.-F. Michel and G. Cathelineau, *International Journal of Inorganic Materials*, 2001, **3**, 87–94.

2 C. Combes, B. Miao, R. Bareille and C. Rey, *Biomaterials*, 2006, **27**, 1945–1954.

3 D. Eichert, C. Drouet, H. Sfihia, C. Rey and C. Combes, in *Biomaterials Research Advances*, Nova Science Publishers, Inc, New York, J.B. Kendall., 2009, vol. 6, pp. 93–143.

4 L. Brečević and A. E. Nielsen, *Journal of Crystal Growth*, 1989, **98**, 504–510.

5 Z. Zou, W. J. E. M. Habraken, G. Matveeva, A. C. S. Jensen, L. Bertinetti, M. A. Hood, C. Sun, P. U. P. A. Gilbert, I. Polishchuk, B. Pokroy, J. Mahamid, Y. Politi, S. Weiner, P. Werner, S. Bette, R. Dinnebier, U. Kolb, E. Zolotoyabko and P. Fratzl, *Science*, 2019, **363**, 396–400.

6 L. Addadi, S. Raz and S. Weiner, *Adv. Mater.*, 2003, **15**, 959–970.

7 B. Myszka, M. Schüßler, K. Hurle, B. Demmert, R. Detsch, A. R. Boccaccini and S. E. Wolf, *RSC Advances*, 2019, **9**, 18232–18244.

8 Y. Fujita, T. Yamamuro, T. Nakamura, S. Kotani, C. Ohtsuki and T. Kokubo, *Journal of Biomedical Materials Research*, 1991, **25**, 991–1003.

9 E. Tolba, W. E. G. Müller, B. M. Abd El-Hady, M. Neufurth, F. Wurm, S. Wang, H. C. Schröder and X. Wang, *J. Mater. Chem. B*, 2016, **4**, 376–386.

10 F. Tewes, O. L. Gobbo, C. Ehrhardt and A. M. Healy, *ACS Appl. Mater. Interfaces*, 2016, **8**, 1164–1175.

11 J. Wei, T. Cheang, B. Tang, H. Xia, Z. Xing, Z. Chen, Y. Fang, W. Chen, A. Xu, S. Wang and J. Luo, *Biomaterials*, 2013, **34**, 1246–1254.

12 O. E. Meiron, E. Bar-David, E. D. Aflalo, A. Shechter, D. Stepensky, A. Berman and A. Sagi, *J Bone Miner Res*, 2011, **26**, 364–372.

13 S. Akhtar, J. E. Barralet, D. Farrar and A. J. Wright, *KEM*, 2006, **309–311**, 179–182.

14 M. Albéric, L. Bertinetti, Z. Zou, P. Fratzl, W. Habraken and Y. Politi, *Adv. Sci.*, 2018, **5**, 1701000.
15 A. Carino, A. Testino, M. R. Andalibi, F. Pilger, P. Bowen and C. Ludwig, *Cryst. Growth Des.*, 2017, **17**, 2006–2015.
16 L. B. Gower and D. J. Odom, *Journal of Crystal Growth*, 2000, **210**, 719–734.
17 Y. Xu, K. C. H. Tijssen, P. H. H. Bomans, A. Akiva, H. Friedrich, A. P. M. Kentgens and N. A. J. M. Sommerdijk, *Nat Commun*, 2018, **9**, 2582.
18 D. Gebauer, A. Völkel and H. Cölfen, *Science*, 2008, **322**, 1819–1822.
19 E. M. Pouget, P. H. H. Bomans, J. A. C. M. Goos, P. M. Frederik, G. de With and N. A. J. M. Sommerdijk, *Science*, 2009, **323**, 1455–1458.
20 F. Sebastiani, S. L. P. Wolf, B. Born, T. Q. Luong, H. Cölfen, D. Gebauer and M. Havenith, *Angew. Chem. Int. Ed.*, 2017, **56**, 490–495.
21 D. Gebauer, P. N. Gunawidjaja, J. Y. P. Ko, Z. Bacsik, B. Aziz, L. Liu, Y. Hu, L. Bergström, C.-W. Tai, T.-K. Sham, M. Edén and N. Hedin, *Angew. Chem. Int. Ed.*, 2010, **49**, 8889–8891.
22 S. Sun, D. M. Chevrier, P. Zhang, D. Gebauer and H. Cölfen, *Angew. Chem. Int. Ed.*, 2016, **55**, 12206–12209.
23 M. Farhadi-Khouzani, D. M. Chevrier, P. Zhang, N. Hedin and D. Gebauer, *Angew. Chem. Int. Ed.*, 2016, **55**, 8117–8120.
24 D. J. Tobler, J. D. Rodriguez-Blanco, K. Dideriksen, N. Bovet, K. K. Sand and S. L. S. Stipp, *Adv. Funct. Mater.*, 2015, **25**, 3081–3090.
25 A. Fernandez-Martinez, B. Kalkan, S. M. Clark and G. A. Waychunas, *Angew. Chem. Int. Ed.*, 2013, **52**, 8354–8357.
26 C. Günther, A. Becker, G. Wolf and M. Epple, *Z. anorg. allg. Chem.*, 2005, **631**, 2830–2835.
27 R. S. K. Lam, J. M. Charnock, A. Lennie and F. C. Meldrum, *CrystEngComm*, 2007, **9**, 1226.
28 S. Sen, D. Kaseman, B. Colas, D. E. Jacob and S. M. Clark, *Phys. Chem. Chem. Phys.*, 2016, **18**, 20330–20337.
29 D. Pontoni, J. Bolze, N. Dingenouts, T. Narayanan and M. Ballauff, *J. Phys. Chem. B*, 2003, **107**, 5123–5125.
30 N. Koga, Y. Nakagoe and H. Tanaka, *Thermochimica Acta*, 1998, **318**, 239–244.
31 Y. Kojima, A. Kawanobe, T. Yasue and Y. Arai, *Nippon Seramikkusu Kyokai gakujutsu ronbunshi*, 1993, **101**, 1145–1152.
32 E. Loste, R. M. Wilson, R. Seshadri and F. C. Meldrum, *Journal of Crystal Growth*, 2003, **254**, 206–218.
33 D. J. Tobler, J. D. Rodriguez Blanco, H. O. Sørensen, S. L. S. Stipp and K. Dideriksen, *Cryst. Growth Des.*, 2016, **16**, 4500–4508.
34 M. A. Bewernitz, D. Gebauer, J. Long, H. Cölfen and L. B. Gower, *Faraday Discuss.*, 2013, **159**, 291–312.
35 Y. Levi-Kalisman, S. Raz, S. Weiner, L. Addadi and I. Sagi, *Adv. Funct. Mater.*, 2002, **12**, 43–48.
36 Y.-P. Lin and P. C. Singer, *Geochimica et Cosmochimica Acta*, 2006, **70**, 2530–2539.
37 Z. Zou, X. Yang, M. Albéric, T. Heil, Q. Wang, B. Pokroy, Y. Politi and L. Bertinetti, *Adv. Funct. Mater.*, 2020, **30**, 2000003.
38 Z. Zou, I. Polishchuk, L. Bertinetti, B. Pokroy, Y. Politi, P. Fratzl and W. J. E. M. Habraken, *J. Mater. Chem. B*, 2018, **6**, 449–457.
39 D. Gebauer, H. Cölfen, A. Verch and M. Antonietti, *Adv. Mater.*, 2009, **21**, 435–439.
40 US20180140631A1, 2018, 35.
41 Y.-P. Lin and P. C. Singer, *Water Research*, 2005, **39**, 4835–4843.
42 L. M. Grover, A. J. Wright, U. Gbureck, A. Bolarinwa, J. Song, Y. Liu, D. F. Farrar, G. Howling, J. Rose and J. E. Barralet, *Biomaterials*, 2013, **34**, 6631–6637.
43 S. M. Naga, M. Awaad, H. F. El-Maghraby and A. M. El-Kady, *Int. J. Appl. Ceram. Technol.*, 2014, **11**, 1–11.
44 J. H. Lee, B.-S. Chang, U.-O. Jeung, K.-W. Park, M.-S. Kim and C.-K. Lee, *Clin. Orthop. Surg.*, 2011, **3**, 238–244.

45 L. Mayen, N. D. Jensen, D. Laurencin, O. Marsan, C. Bonhomme, C. Gervais, M. E. Smith, C. Coelho, G. Laurent, J. Trebosc, Z. Gan, K. Chen, C. Rey, C. Combes and J. Soulié, *Acta Biomaterialia*, 2019, S1742706119308566.
46 P. Juhás, T. Davis, C. L. Farrow and S. J. L. Billinge, *J Appl Cryst*, 2013, **46**, 560–566.
47 C. L. Farrow, P. Juhas, J. W. Liu, D. Bryndin, E. S. Božin, J. Bloch, T. Proffen and S. J. L. Billinge, *J. Phys.: Condens. Matter*, 2007, **19**, 335219.
48 C. R. Morcombe and K. W. Zilm, *Journal of Magnetic Resonance*, 2003, **162**, 479–486.
49 D. G. Cory and W. M. Ritchey, *Journal of Magnetic Resonance*, 1988, **80**, 128–132.
50 O. F. Yasar, W.-C. Liao, B. Stevensson and M. Edén, *J. Phys. Chem. C*, 2021, **125**, 4675–4693.
51 G. Metz, X. L. Wu and S. O. Smith, *Journal of Magnetic Resonance, Series A*, 1994, **110**, 219–227.
52 B. M. Fung, A. K. Khitrin and K. Ermolaev, *Journal of Magnetic Resonance*, 2000, **142**, 97–101.
53 D. Massiot, F. Fayon, M. Capron, I. King, S. Le Calvé, B. Alonso, J.-O. Durand, B. Bujoli, Z. Gan and G. Hoatson, *Magn. Res. Chem.*, 2002, **40**, 70–76.
54 J. D. Rodriguez-Blanco, S. Shaw and L. G. Benning, *Mineral. mag.*, 2008, **72**, 283–286.
55 S. Leukel, M. Panthöfer, M. Mondeshki, G. Kieslich, Y. Wu, N. Krautwurst and W. Tremel, *J. Am. Chem. Soc.*, 2018, **140**, 14638–14646.
56 P. Gras, C. Rey, O. Marsan, S. Sarda and C. Combes, *Eur. J. Inorg. Chem.*, 2013, **2013**, 5886–5895.
57 D. J. Sutor and J. M. Percival, *Clinica Chimica Acta*, 1978, **89**, 479–484.
58 N. Chhim, Institut National Polytechnique de Toulouse (INP Toulouse), 2019.
59 Q. Feng, *Progress in molecular and subcellular biology*, 2011, **52**, 141–97.
60 R. Sun, C.-W. Tai, M. Strømme and O. Cheung, *Microporous and Mesoporous Materials*, 2020, **292**, 109736.
61 R. Sun, P. Zhang, É. G. Bajnóczi, A. Neagu, C.-W. Tai, I. Persson, M. Strømme and O. Cheung, *ACS Appl. Mater. Interfaces*, 2018, **10**, 21556–21564.
62 A. V. Radha, T. Z. Forbes, C. E. Killian, P. U. P. A. Gilbert and A. Navrotsky, *PNAS*, 2010, **107**, 16438–16443.
63 F. Konrad, F. Gallien, D. E. Gerard and M. Dietzel, *Cryst. Growth Des.*, 2016, **16**, 6310–6317.
64 Z. Zou, L. Bertinetti, Y. Politi, A. C. S. Jensen, S. Weiner, L. Addadi, P. Fratzl and W. J. E. M. Habraken, *Chem. Mater.*, 2015, **27**, 4237–4246.
65 H. Du, M. Steinacher, C. Borca, T. Huthwelker, A. Murello, F. Stellacci and E. Amstad, *J. Am. Chem. Soc.*, 2018, **140**, 14289–14299.
66 L. Boldon, F. Laliberte and L. Liu, *Nano Reviews*, 2015, **6**, 25661.
67 A. F. Wallace, L. O. Hedges, A. Fernandez-Martinez, P. Raiteri, J. D. Gale, G. A. Waychunas, S. Whitelam, J. F. Banfield and J. J. D. Yoreo, *Science*, 2013, **341**, 885–889.
68 B. Colas, Macquarie University, 2017.
69 T. Egami and S. J. L. Billinge, *Underneath the Bragg Peaks: Structural Analysis of Complex Materials*, Newnes, 2012.
70 O. Masson and P. Thomas, *J Appl Cryst*, 2013, **46**, 461–465.
71 M. W. Terban and S. J. L. Billinge, *Chem. Rev.*, 2022, **122**, 1208–1272.
72 D. L. Graf, *American Mineralogist*, 1961, **46**, 1283–1316.
73 R. Demichelis, P. Raiteri, J. D. Gale and R. Dovesi, *CrystEngComm*, 2012, **14**, 44–47.
74 M. P. Schmidt, A. J. Ilott, B. L. Phillips and R. J. Reeder, *Cryst. Growth Des.*, 2014, **14**, 938–951.
75 F. M. Michel, J. MacDonald, J. Feng, B. L. Phillips, L. Ehm, C. Tarabrella, J. B. Parise and R. J. Reeder, *Chem. Mater.*, 2008, **20**, 4720–4728.
76 J. H. E. Cartwright, A. G. Checa, J. D. Gale, D. Gebauer and C. I. Sainz-Díaz, *Angew. Chem. Int. Ed.*, 2012, **51**, 11960–11970.
77 Y. Politi, Y. Levi-Kalisman, S. Raz, F. Wilt, L. Addadi, S. Weiner and I. Sagi, *Adv. Funct. Mater.*, 2006, **16**, 1289–1298.
78 A. B. Rodríguez-Navarro, P. Marie, Y. Nys, M. T. Hincke and J. Gautron, *Journal of Structural Biology*, 2015, **190**, 291–303.
79 B. Hasse, H. Ehrenberg, J.-C. Marxen, W. Becker and M. Epple, *Chem. Eur. J.*, 2000, **6**, 3679–3685.

80 P. Gras, A. Baker, C. Combes, C. Rey, S. Sarda, A. J. Wright, M. E. Smith, J. V. Hanna, C. Gervais, D. Laurencin and C. Bonhomme, *Acta Biomaterialia*, 2016, **31**, 348–357.
81 H. Du and E. Amstad, *Angew. Chem. Int. Ed.*, 2020, **59**, 1798–1816.
82 Y. Wang, S. Von Euw, F. M. Fernandes, S. Cassaignon, M. Selmane, G. Laurent, G. Pehau-Arnaudet, C. Coelho, L. Bonhomme-Coury, M.-M. Giraud-Guille, F. Babonneau, T. Azaïs and N. Nassif, *Nature Mater*, 2013, **12**, 1144–1153.
83 C. Slater, D. Laurencin, V. Burnell, M. E. Smith, L. M. Grover, J. A. Hriljac and A. J. Wright, *J. Mater. Chem.*, 2011, **21**, 18783.
84 S. Kababya, A. Gal, K. Kahil, S. Weiner, L. Addadi and A. Schmidt, *J. Am. Chem. Soc.*, 2015, **137**, 990–998.
85 A. Al-Sawalmih, C. Li, S. Siegel, P. Fratzl and O. Paris, *Adv. Mater.*, 2009, **21**, 4011–4015.
86 S. M. Clark, B. Colas, D. E. Jacob, J. C. Neuefeind, H.-W. Wang, K. L. Page, A. K. Soper, P. I. Schodder, P. Duchstein, B. A. Zubiri, T. Yokosawa, V. Pipich, D. Zahn, E. Spiecker and S. E. Wolf, *Sci Rep*, 2022, **12**, 6870.

Supplementary Information

Pyrophosphate-stabilised amorphous calcium carbonate for bone substitution: toward a doping-dependent cluster-based model

Marion Merle[1], Jérémy Soulié[1], Capucine Sassoye[2], Pierre Roblin[3], Christian Rey[1], Christian Bonhomme[2], Christèle Combes[1,*]

1. CIRIMAT, Université de Toulouse, CNRS, TOULOUSE INP - ENSIACET, Toulouse, France
2. Sorbonne Université, CNRS, LCMCP, Paris, France
3. LGC, CNRS, Université de Toulouse, 118 route de Narbonne Bâtiment 2R1, Toulouse, France

A. Pyrophosphate precursor

The XRD diagram and FTIR spectrum of the sodium pyrophosphate precursor are presented Figure S1. The attribution of the FTIR bands is done according to Gras's work.[1]

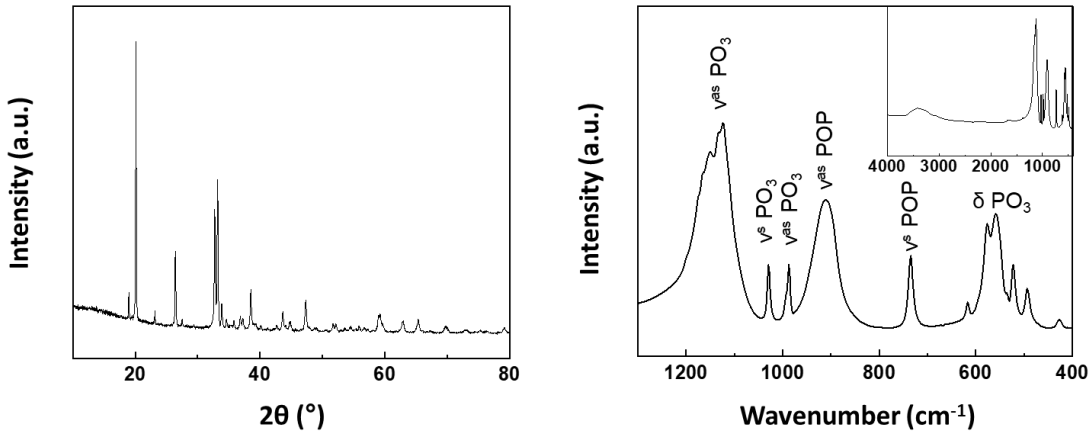

Figure S1: XRD diagram (left) and FTIR spectrum (right) of the synthesised sodium pyrophosphate precursor used for the synthesis of the zPyACC powders.

B. FTIR spectroscopy analysis of the ^{13}C-enriched zPyACC samples

A shift of the carbonate vibration bands in FTIR spectrum (Figure S2) confirmed the quasi-total enrichment in ^{13}C of the powder. Indeed, the ν_2CO_3 at 865 cm^{-1} in 10PyACC and in 5PyACC was totally shifted at 838 cm^{-1} for 10PyACC13 and 5PyACC13 samples. This shift (experimental ratio of 0.969) is in accordance with Rey *et al.*,[2] stating that for the ν_2CO_3 vibration the line position ratio is 0.9686. It is also in agreement with the shift obtained by Xu *et al.*[3] for the ν_2 vibration of 100% ^{13}C enriched calcite ($\nu_2{}^{12}CO_3$ at 877 cm^{-1} and $\nu_2{}^{13}CO_3$ at 850 cm^{-1}).

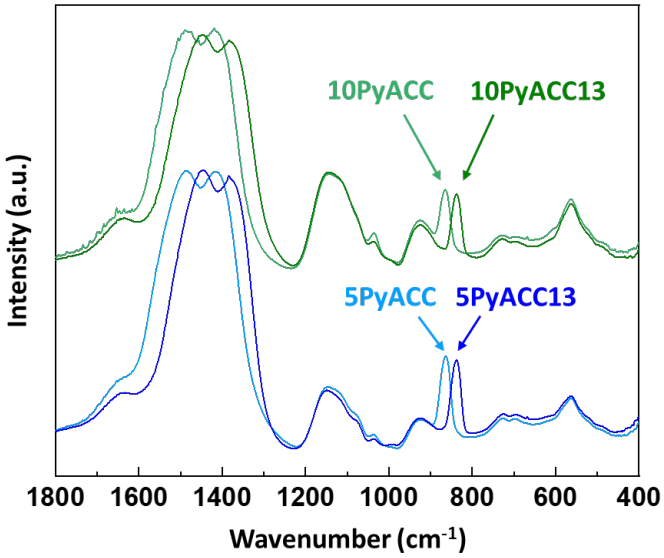

Figure S2: FTIR spectra of the 10PyACC and 5PyACC and their corresponding ^{13}C enriched powders, 10PyACC13 and 5PyACC13 respectively.

C. Raman spectra of the zPyACC powders

Raman spectroscopy analysis was done using a Raman Labram HR 800 confocal microscope Horiba Jobin Yvon, with a continuous 532 nm argon diode laser and a power of 8 mW. Samples were observed with a BX 41 Olympus microscope equipped with a x100 lens, conferring a spatial resolution of 0.7 µm and an axial resolution (penetration length) of 2.6 µm. Spectra were collected with a spectral resolution of 1.5 cm^{-1}, thanks to the grating of 600 lines per mm. Each spectrum was recorded with an integration time of 60 s and 3 accumulations.

The vibration bands corresponding to the carbonate and pyrophosphate groups can be observed in the Raman spectra (Figure S3).[4,5] The major carbonate band, corresponding to the symmetric stretching vibration v_1CO_3, at 1085 cm^{-1} in the calcite (0PyACC) is shifted to 1081 cm^{-1} in ACC. The smaller bands associated to v_3CO_3 and v_4CO_3 are respectively at 1437 cm^{-1} and 712 cm^{-1} in calcite, but much less pronounced or undetectable in ACC as the lattice bands below 400 cm^{-1} which are also not detectable in ACC. Concerning the pyrophosphate, the main band, attributed to v^sPO_3 and located at 1040 cm^{-1}, is characteristic of amorphous calcium pyrophosphate (aCPP).[1] The v^sPOP vibration, at 732 cm^{-1}, is also attributed to aCPP.

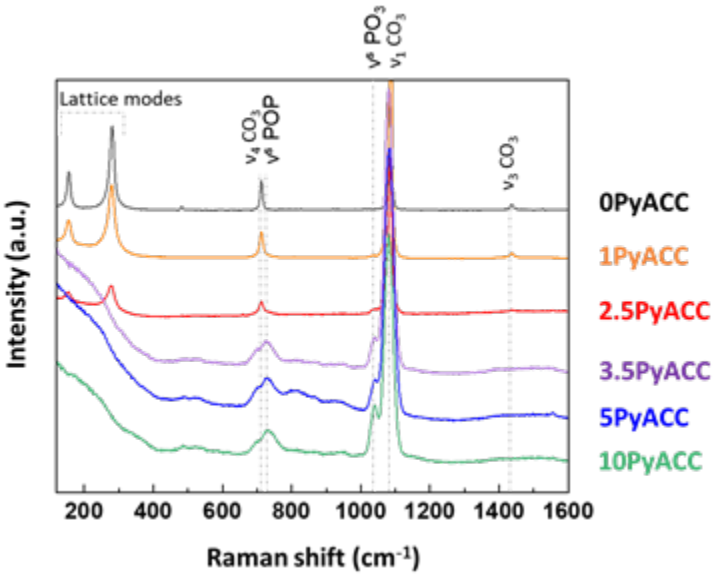

Figure S3: Raman spectra of the various zPyACC synthesised powders, with the associated carbonate and pyrophosphate vibrations identified.

D. Thermogravimetric analysis

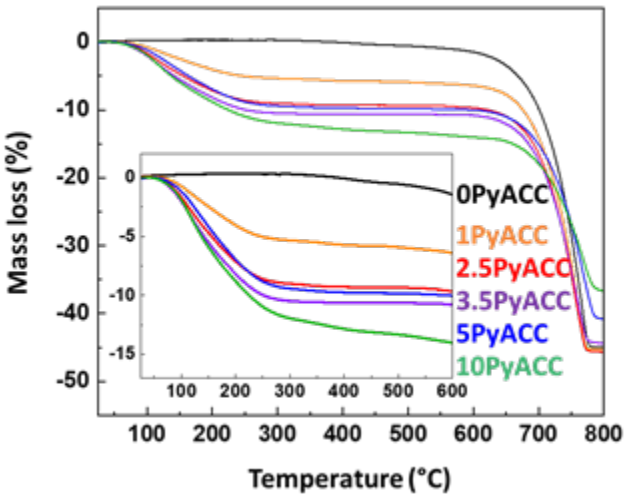

Figure S4: TGA curves of the zPyACC samples heated from 25°C to 800°C in air at a rate of 5°C/min.

E. Differential Thermal Analysis

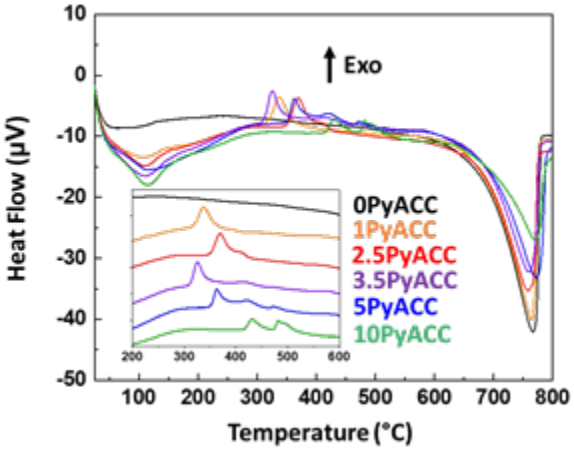

Figure S5: DTA curves of the synthesised zPyACC samples heated from 25°C to 800°C in air at a rate of 5°C/min. The curves are shifted in the inset for better clarity.

F. EDS mapping methodology and analysis movie

During the EDS analysis of the 5PyACC powder, the incident electron beam caused the water radiolysis as described by Du *et al.*[6] and the water contained in the nanoparticle transformed into water vapour and formed an entrapped bubble into the resin. We saw this bubble moving within the particle without any modification of the external shape of the latter, during the 6 min of EDS analysis. The attached movie was created by the succession of all of the 60 frames of the analysis. The dimensions of the picture are 130 nm x 130 nm.

Oxygen, phosphorus and calcium distributions into the 5PyACC particle determined by EDS analysis (Figures 5d, 5e, 5f) could appear inhomogeneous, unlike what we discussed in the main text of the article. In fact, calcium and oxygen seemed concentrated to the upper left part of the particle but it was related to the presence of the gas bubble at the bottom right and the low content of pyrophosphate. As EDS is also sensitive to the volume, for O and Ca we detected atoms from the upper surface of the spherical particle, but also from the lower surface after crossing the internal volume of the particle, except for the bottom right part that was masked by the gas bubble. But for P, as there was a lower content, with such a brief analysis (necessary to avoid strong alteration of the sample), we only collected the signal coming from the P atoms present at the upper surface of the particle, and not from the lower surface, leading to a distribution that appeared homogeneous despite the presence of the gas bubble.

G. SAXS fitting

The software SASView was used for fitting the SAXS curves. In this whole section, the uncertainties given are coming from the fitting process. To determine the first characteristic dimension D_1, two power law models with a $I(q) = k.q^{-p}$ equation type were created. The first power law, adjusted on the first 6 points of the curve, was $I_{pl1}(q) = 0.18q^{-2.114}$ for 10PyACC. The second one, adjusted to the main slope at the intermediate angles, was $I_{pl2}(q) = 4.98.10^{-5}q^{-3.9587}$. The intersection point of both lines was calculated at q_1 = 0.0121 Å^{-1}, *i.e.* with $q_1 = 2\pi/D_1$, D_1 = 51.9 $\pm$ 0.2 nm. Then, in order to exacerbate the hump and make the fitting easier, the second power law $I_{pl2}(q)$ was subtracted to the data. The first

attempt for fitting was done using a Gaussian peak model $I_{Gp}(q) = k.\exp\left[\frac{-\frac{1}{2}(q-q_0)^2}{\sigma^2}\right]$, with the peak being centered at q_0 and having a standard deviation of σ. After an adjustment of the initial parameters by hand, the fitted parameters were R_{2Gp} = 3.38 $\pm$ 0.01 nm with σ = 0.03 for 10PyACC. The fitting was refined using a hardsphere structure factor added to a sphere model, to take into account the interactions between the close spheres. The equation, given in the Materials and Methods part, was applied with a scattering length density of calcite (for the clusters) of $2.57.10^{-5}$ Å^{-2} (really close to the vaterite one: $2.41.10^{-5}$ Å^{-2}) and of water of $9.48.10^{-6}$ Å^{-2}. After a manual adjustment of the initial parameters it gave the following fitted parameters for 10PyACC: $R_{2s.hs}$ = 2.485 $\pm$ 0.008 nm with a 14 % polydispersity, R_{2eff} = 3.70 $\pm$ 0.01 nm with a 10 % polydispersity and volume fraction = 0.697 $\pm$ 0.005. The effective radius R_{2eff} is the distance between the centre of the sphere and the centre of the distance between two spheres, *i.e.* 2 R_{2eff}, is equal to the distance between the centres of two-neighbour spheres. It was really close to the R_{2Gp} obtained with the Gaussian peak model; consequently, we concluded that the latter was taking into account a part of the sphere-sphere interactions and not strictly the cluster radius. That is why we decided to focus mainly on the $R_{2s.hs}$ value, obtained with the sphere model, probably more accurate for the clusters size.

For identifying the peaks present in the WAXS curves, the JCPDS data of calcite (00-005-0586), vaterite (hexagonal, 01-072-0506), aragonite (01-071-2392) and monohydrocalcite (01-076-7969) were used. Their corresponding 2θ were converted in q values using the following equation: $q = \frac{4\pi \sin\theta}{\lambda}$ (with λ = 1.5 Å), then the curves were plotted and compared to the zPyACC WAXS2D curves. For clarity, we showed only the comparison with calcite and vaterite (the other crystalline phases having no common peaks).

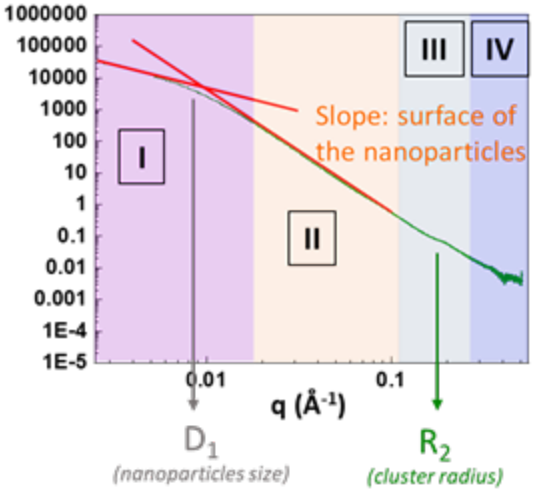

Figure S6: Explanation of the analysis method developed to fit the SAXS curves. The first dimension D_1 in the domain I can be calculated from the coordinates of the intersection point of the tangent to the curve (modelled by power laws). The slope in the domain II gave information on the nanoparticles surface. Then, the cluster radius R_2 in the domain III was obtained by fitting the hump.

H. Pair Distribution Function analysis

The reduced atomic PDF, G(r), gives, from a **structural model**, the probability of finding a pair of atoms at a distance r as follows:[7–12]

$$G(r) = 4.\pi.\ [\rho(r) - \rho_0]$$

where ρ(r) is the atomic pair-density and ρ_0 is the average atomic number density.

As defined, peaks in the G(r) function correspond to specific distances separating a pair of atoms. G(r) can also be **extracted from an experimental XRD** pattern. Indeed, G(r) is the *sine* Fourier Transform of the reduced total scattering structure function F(Q):

$$F(Q) = Q.(S(Q)-1)$$

$$G(r) = \frac{2}{\pi}\int_0^{Qmax} Q.[S(Q)-1].\sin(Q.r)\,.dQ$$

where Q is the magnitude of the scattering vector ($Q = 4\pi \sin\left(\frac{\theta}{\lambda}\right)$), 2θ being the angle between the incoming and outgoing X-ray, λ is the X-ray wavelength, and S(Q) is the total scattering structure function which is the corrected and normalised experimental measured intensity.

Thus, PDF analysis provides information regarding inter-atomic distances leading to the local structure, for both crystalline and amorphous materials. When possible, the successful comparison between calculated and experimental G(r) leads to the structural modal validation.

SI-H1: Crystalline calcite and vaterite refinements.

Crystalline calcite and vaterite were synthesised as reference samples. Their local structures were refined allowing the cell parameters, isotropic atomic displacements, atomic positions and broadening factors to vary.

We used the Graf. D.L's published structure[13] for calcite. Concerning vaterite many structural models exist. We have carefully read Burgess[14] work who has been using DFT calculations, DRX and NMR data to compare all and select the two most probable structures. We attempted refinement from both models. The $P3_221$ model[15] presented a too high number of parameters to allow processing the refinement. We thus pursued our work with the C2 model[16] which allowed refinement using all parameters. This led to good reliability factors of 12.9 % for calcite and 10.9 % for vaterite, thus validating the structural models and our PDF setup.

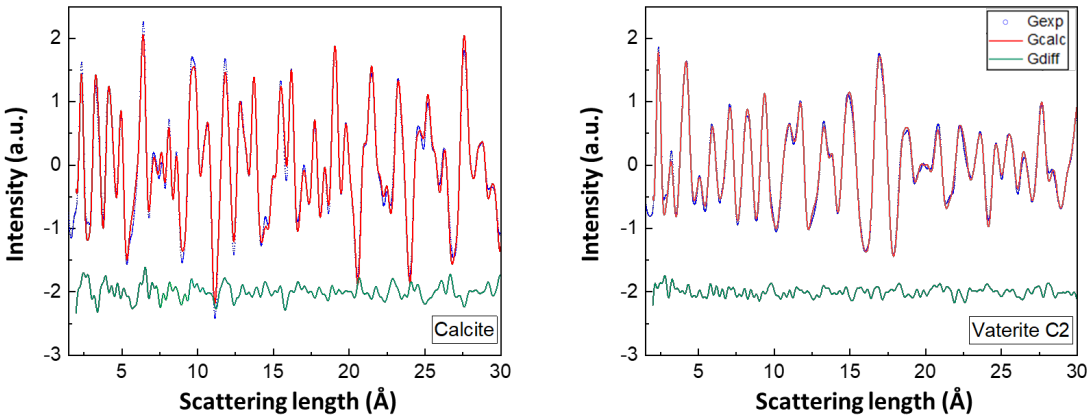

Figure S7: Experimental (blue circles), calculated (red line) and differential (green line) G(r) curves for calcite and monoclinic C2 vaterite

SI-H2: Experimental coherent length from PDF analysis

The coherence length, meaning the maximum distance for which the atoms are organised according to a single structure, could be determined from experimental PDF curve. This corresponded to the maximum r value for which PDF peaks could still be distinguished from the background oscillations, as illustrated in Figure S8. Table S1 presents the coherence length extracted from the PDF curves.

Table S1: Coherence length of the zPyACC determined by PDF analysis.

Samples	Coherence length (nm)
1PyACC	55-60
2.5PyACC	50-55
3.5PyACC	1
5PyACC	1
10PyACC	1

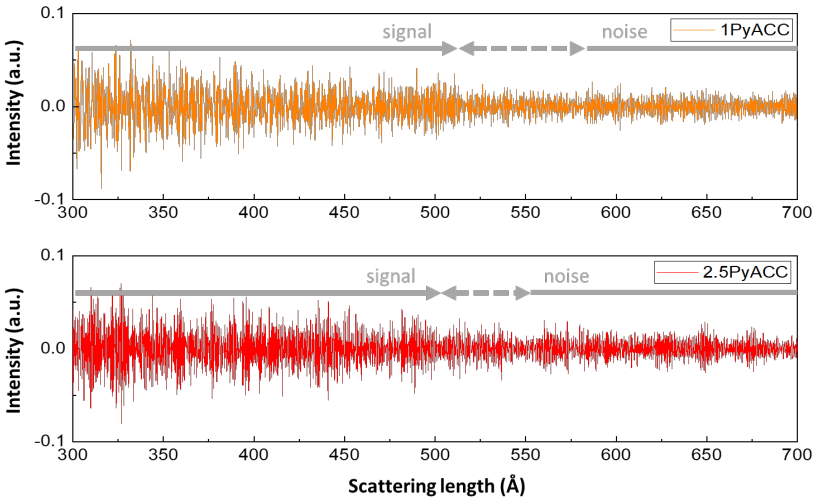

Figure S8: Experimental PDF curves (Gexp(r)) at larger r scales, for 1PyACC (top) and 2.5PyACC (bottom), showing their coherence length between 50 and 60 nm, above which the signal cannot be distinguished from the noise.

SI-H3: Calculation of amorphous calcite and vaterite

Refined parameters from refined crystalline calcite and vaterite were used, combined with a dampening factor of 9 Å to mimic the absence of organisation at high distances in the amorphous phases. Even at small distances, amorphous calcite and amorphous vaterite had different signatures and thus could be distinguished (Figure S9).

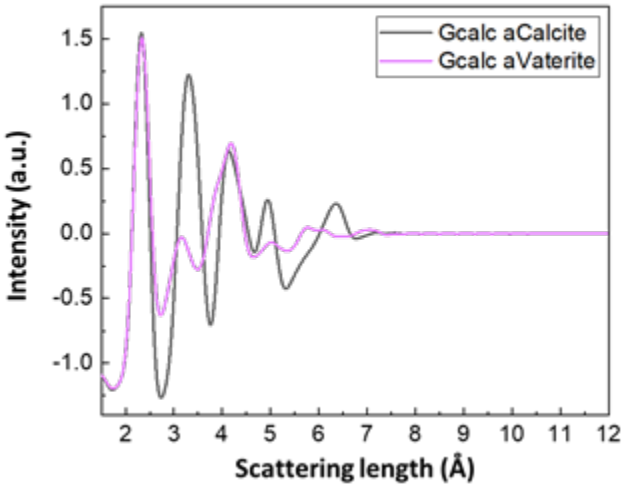

Figure S9: Comparison of the calculated PDF curves (Gcalc(r)) for amorphous calcite (aCalcite) and amorphous vaterite (aVaterite)

SI-H4: The amorphous phase in 1PyACC and 2.5PyACC samples

Both experimental 1PyACC and 2.5PyACC PDF curves only presented peaks at distances corresponding to calcite. However, intensities for 2.5PyACC sample declined faster with r that for the 1PyACC one or crystalline calcite, which made it harder to compare and interpret (Figure S10a). We normalised the three curves based on the 27.6 Å peaks. It showed that all samples presented the same structure, calcite, at high distances, but that an additional amorphous phase was also present at small order, below 9 Å (Figure S10b). Subtractions of the normalised curves (G_{exp}(r)1PyACC - G_{exp}(r)calcite and G_{exp}(r)2.5PyACC - G_{exp}(r)calcite) gave a similar signal (peaks at the same distances), with higher intensities for 2.5PyACC than for 1PyACC (Figure S10c). Normalisation based on the first peak showed that both normalised differences were equal, meaning that a similar amorphous phase (named a1PyACC and a2.5PyACC) was obtained in addition to crystalline calcite, when Py was present during precipitation (Figure S10d): the more Py initially in solution, the more amorphous phase was present in the synthesised powder.

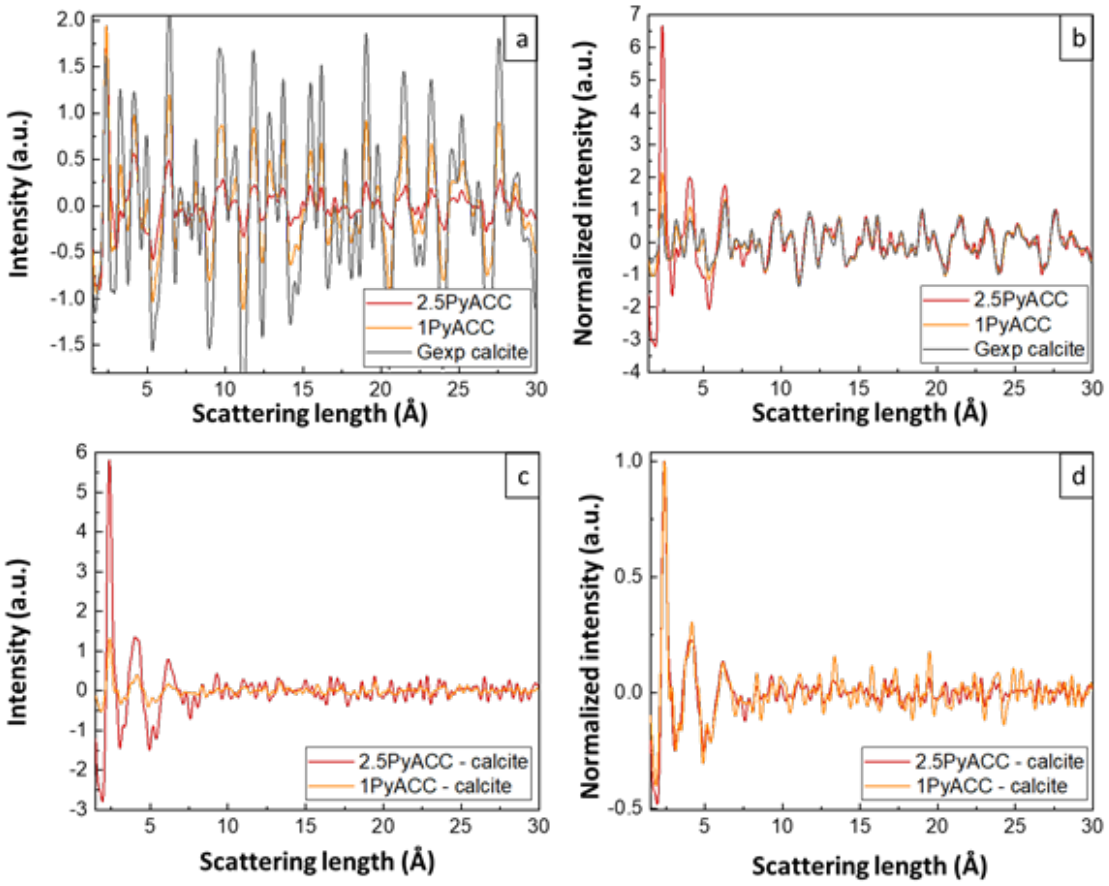

Figure S10: Comparison of the experimental Gexp(r) curves of 2.5PyACC, 1PyACC and calcite without normalisation (a) and after a normalisation by the 27.6 Å peak (b). Gexp(r)1PyACC - Gexp(r)calcite and Gexp(r)2.5PyACC - Gexp(r)calcite curves without additional normalisation (c) and with a normalisation by the first peak (d).

SI-H5: Comparison between amorphous calculated calcite and experimental amorphous 3.5PyACC, 5PyACC and 10PyACC

The amorphous 3.5PyACC, 5PyACC and 10PyACC Gexp(r) curves presented a large peak at 3.8 Å (blue arrow in Figure S11) that could not be reproduced with amorphous calculated calcite. Similarly, the intense peak at 3.3 Å of amorphous calculated calcite did not match with the amorphous 3.5PyACC, 5PyACC and 10PyACC Gexp(r) curves (grey arrow in Figure S11). We could not validate the calcite structure as a conceivable model.

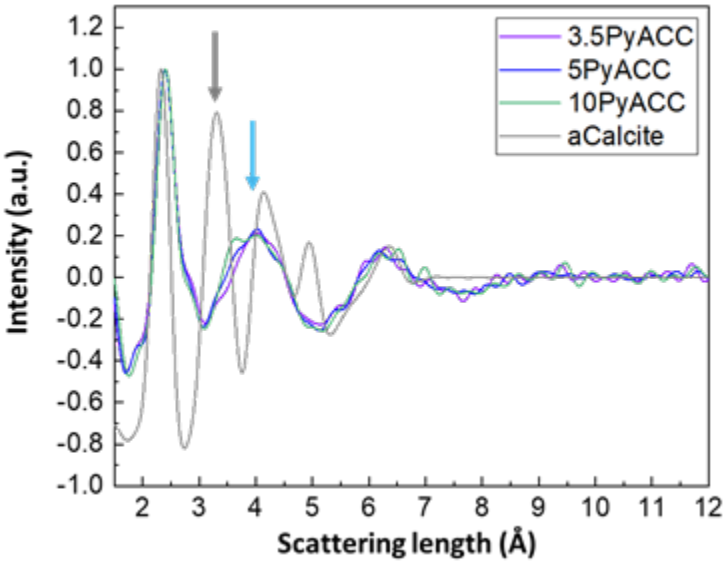

Figure S11: Comparison of the Gexp(r) of the fully amorphous zPyACC samples (3.5PyACC, 5PyACC and 10PyACC) and the Gcalc(r) of the amorphous calcite (aCalcite).

I. NMR ^{13}C CP MAS spectra of 5PyACC13 and 10PyACC13 samples

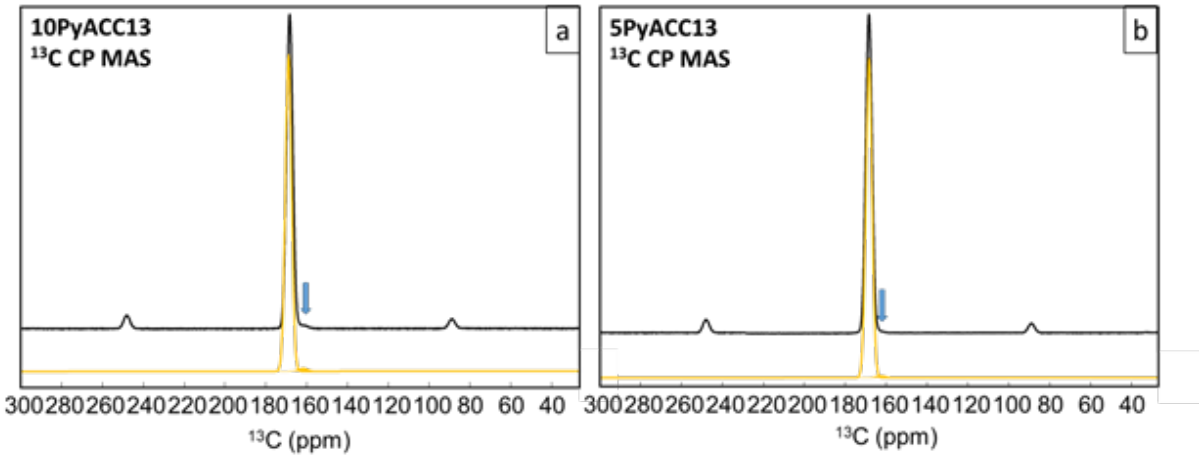

Figure S12: ^{13}C CP MAS spectra of 10PyACC13 ***(a)*** *and 5PyACC13* ***(b)****. The DMFit simulations are shown in orange. The major component corresponds to CO_3^{2-} species whereas the very minor one (plain, orange) corresponds to HCO_3^- species. The associated parameters are given in the main text.*

Bibliography

1 P. Gras, C. Rey, O. Marsan, S. Sarda and C. Combes, *Eur. J. Inorg. Chem.*, 2013, **2013**, 5886–5895.
2 C. Rey, O. Marsan, C. Combes, C. Drouet, D. Grossin and S. Sarda, in *Advances in Calcium Phosphate Biomaterials*, ed. B. Ben-Nissan, Springer Berlin Heidelberg, Berlin, Heidelberg, 2014, vol. 2, pp. 229–266.
3 B. Xu, A. Hirsch, L. Kronik and K. M. Poduska, *RSC Advances*, 2018, **8**, 33985–33992.
4 G. Behrens, L. T. Kuhn, R. Ubic and A. H. Heuer, *Spectroscopy Letters*, 1995, **28**, 983–995.
5 L. Mayen, N. D. Jensen, D. Laurencin, O. Marsan, C. Bonhomme, C. Gervais, M. E. Smith, C. Coelho, G. Laurent, J. Trebosc, Z. Gan, K. Chen, C. Rey, C. Combes and J. Soulié, *Acta Biomaterialia*, 2019, S1742706119308566.
6 H. Du, M. Steinacher, C. Borca, T. Huthwelker, A. Murello, F. Stellacci and E. Amstad, *J. Am. Chem. Soc.*, 2018, **140**, 14289–14299.
7 T. Egami and S. J. L. Billinge, *Underneath the Bragg Peaks: Structural Analysis of Complex Materials*, Newnes, 2012.
8 O. Masson and P. Thomas, *J Appl Cryst*, 2013, **46**, 461–465.
9 S. J. L. Billinge and M. G. Kanatzidis, *Chemical Communications*, 2004, **0**, 749–760.
10 V. Petkov, *Materials Today*, 2008, **11**, 28–38.
11 C. L. Farrow and S. J. L. Billinge, *Acta Cryst A*, 2009, **65**, 232–239.
12 M. W. Terban and S. J. L. Billinge, *Chem. Rev.*, 2022, **122**, 1208–1272.
13 D. L. Graf, *American Mineralogist*, 1961, **46**, 1283–1316.
14 K. M. N. Burgess and D. L. Bryce, *Solid State Nuclear Magnetic Resonance*, 2015, **65**, 75–83.
15 R. Demichelis, P. Raiteri, J. D. Gale and R. Dovesi, *CrystEngComm*, 2012, **14**, 44–47.
16 R. Demichelis, P. Raiteri, J. D. Gale and R. Dovesi, *Cryst. Growth Des.*, 2013, **13**, 2247–2251.